Construction and Building Materials 459 (2025) 139767

Contents lists available at ScienceDirect

Construction and Building Materials

journal homepage: www.elsevier.com/locate/conbuildmat

Utilisation of simulation-driven fibre orientation for effective modelling of flexural strength and toughness in self-compacting concrete

Abdullah Alshahrani [a,*], Sivakumar Kulasegaram [b,*], Abhishek Kundu [b]

[a] Department of Civil Engineering, College of Engineering, Najran University, Najran, Saudi Arabia
[b] School of Engineering, Cardiff University, Cardiff, UK

ARTICLE INFO

Keywords:
Self-compacting concrete
Steel fibre-reinforced concrete (SFRC)
Fibre orientation
Flexural strength
Toughness
Finite element modelling (FEM)
Post-cracking behaviour

ABSTRACT

The design of concrete elements reinforced with steel fibres should consider not only strength criteria but also residual tensile strength and post-peak behaviour, and the resulting improvement in toughness. This paper introduces an innovative finite element modelling approach to simulate the flexural properties and post-cracking performance of self-compacting concrete (SCC) reinforced with steel fibres, considering varying fibre orientations and distributions. The concrete matrix was modelled in ABAQUS using the damage plasticity model, with automated fibre distribution and orientation, evaluating SCC flow-based, random, and longitudinal span alignment of the fibres. Numerical simulations of plain and reinforced SCC were validated using three-point bending tests on notched prism specimens in accordance with ASTM C1609. Further simulations assessed the impact of fibre orientation on the flexural strength and toughness of reinforced concrete, comparing random and longitudinal fibre alignments. The simulation results for plain SCC and fibre-reinforced SCC with fibre orientation based on the flow of SCC closely matched the average experimental curve, demonstrating a high degree of accuracy. Furthermore, the results indicated that longitudinal alignment of fibres can enhance flexural strength and toughness by up to 104.4 % and 127.1 %, respectively, compared to a random fibre orientation in fibre-reinforced SCC.

1. Introduction

The low tensile strength and brittleness of plain concrete present significant challenges, restricting its use in structural applications [1,2]. Incorporating steel fibres into cementitious composites improves ductility and post-peak performance by bridging cracks, limiting propagation, and enhancing energy absorption. Although the compressive strength remains largely unaffected, the addition of steel fibres significantly increases toughness, residual tensile strength, and flexural strength [3]. These enhancements have facilitated the widespread adoption of steel fibre-reinforced cementitious composites (SFR-CC) in both research and engineering practice, where steel fibres are commonly employed as primary or secondary reinforcement in compliance with established design standards [4–9].

Reinforcing cementitious materials with steel fibres can significantly improve its mechanical characteristics, including toughness, ductility, and flexural, shear, and tensile strengths, as well as its shrinkage behaviour and durability [10,11]. The contribution of steel fibres to the structural integrity of reinforced concrete structures is not limited to merely strengthening fundamental material properties of SFR-CC. This also enhances the seismic resilience of framed buildings, fatigue strength under cyclic loading and torsional strength of beams, as is evidenced by extensive research [12–14].

The effectiveness of SFR-CC in strengthening concrete structures largely depends on the alignment and distribution of steel fibres relative to external loads [1,15–18]. Research [16,19,20] has shown that steel fibres within concrete structures often display a random orientation in Steel Fibre Reinforced Concrete (SFRC) due to factors such as the rheological properties of the concrete, vibration, casting methods, placement methods, and more. This randomness makes SFRC particularly well-suited for structural elements exposed to multidirectional forces, such as precast roof elements [21] and shell roofs [22]. However, for structural components as beams, which are primarily subject to unidirectional forces, a uniform alignment of fibres along the direction of tensile stress is crucial. Generally, the random and nonuniform distribution of steel fibres can limit the broader application of SFRC. Research reported in[16] has indicated that merely increasing the quantity of fibres in SFRC beams does not necessarily enhance their

* Corresponding authors.
E-mail addresses: aalshahranie@nu.edu.sa (A. Alshahrani), kulasegarams@cardiff.ac.uk (S. Kulasegaram).

https://doi.org/10.1016/j.conbuildmat.2024.139767
Received 12 October 2024; Received in revised form 9 December 2024; Accepted 23 December 2024
Available online 31 December 2024

flexural performance, as the fibres do not consistently distribute or align along the tension lines within the concrete matrix. Therefore, it is crucial to explore alternative appropriate strategies to achieve better alignment and distribution of the fibres, aiming to enhance the flexural strength of SFRC- beams [17,23].

In addition, the mechanical effectiveness of SFR-CC is profoundly influenced by the interfacial interaction between fibre and concrete, especially due to the phenomenon of fibre pull-out, a pivotal factor in the crack-bridging capacity of fibres [24]. As a result, extensive research, including experimental, theoretical, and computational analyses, has been conducted to investigate the crucial bond-slip interaction at the fibre-matrix interface [25–42]. Furthermore, for structural design purposes, established empirical methods have been developed to calculate the properties of SFR-CC [43]. Despite considerable advancements in experimental and theoretical research on SFR-CC, numerical studies still exhibit shortcomings. This is primarily because the bridging effect, attributed to fibre pull-out behaviour, is often over-simplified, and typically incorporated only as part of the constitutive model of plain concrete [24].

Scholars have developed various numerical models to simulate the fracture behaviour of SFR-CC, broadly classified into two types based on the treatment of steel fibres: macro-simulation (continuous type) [44–47], and meso-simulation (discrete type) [48–53]. In macro-simulation, SFR-CC is conceptualised as a homogeneous composite, with the reinforcement effect of steel fibres incorporated by modifying parameters within the constitutive model of plain concrete. For instance, Chi et al. [44] modified the concrete damaged plasticity model to simulate mechanical responses of fibre reinforced concrete (FRC) materials under multiaxial loading conditions and to evaluate the seismic behaviour of FRC columns under cyclic loading scenarios. Bi et al. [45] modified the smeared crack constitutive model of plain concrete, incorporating the bond-slip relationship between fibres and the concrete matrix, to simulate the uniaxial tensile behaviour of FRC. Although theses continuous models are probably capable to simulate the post-cracking characteristics, an explicit illustration of fibre distribution and orientation is not provided, and complex coding is typically required for development.

Advancements in numerical simulation have enabled researchers to develop models incorporating discrete fibres to simulate the mechanical behaviour of SFR-CC. These models treat SFR-CC as a biphasic composite, comprising a cementitious matrix and steel fibres, each governed by distinct constitutive laws. For instance, Xu et al. [48] developed a two-dimensional mesoscale model that incorporates fibres, aggregates, and mortar to investigate the dynamic tensile behaviour of SFRC. However, this model does not account for the bond-slip relationship between the fibres and the mortar, which is critical for accurate post-cracking simulations. Zhang et al. [37] developed a discrete continuum coupled model for SFRC using an isotropic damage model for the concrete matrix and a perfect elastoplastic model for the steel fibres. Cohesive interface elements were introduced to simulate bond-slip interactions; however, the need to match the mesh between the fibre and matrix for computational convergence significantly increases computational time, limiting the number of fibres included in the model [54].

Cunha et al. [49,50] developed a finite element approach that incorporates discrete steel fibres to simulate the tensile and flexural behaviour of Steel Fibre Reinforced Self-Compacting Concrete (SFR-SCC). In their approach, the interaction between the steel fibres and the matrix was modelled as a rigid coupling (perfect bond), eliminating the need for mesh alignment between the fibres and the matrix. The bond-slip relationship between the steel fibres and the matrix is considered indirectly, by using the pull-out response of steel fibres to define the stress-strain relationship of the fibres. In a similar vein, Yu et al. [51] and Pros et al. [55] applied a comparable approach to model the bond-slip relationship of fibres, relying on the analytical expressions derived from the pull-out responses of steel fibres. Typically, these models utilise algorithms to establish a fibre distribution, which is delineated through statistical methods. Numerical models that explicitly incorporate discrete fibres have been instrumental in enhancing the understanding of SFR-CC behaviour. Such an advanced understanding is attainable through the simulation of diverse scenarios, encompassing variations in fibre properties, content, orientation and distribution.

In many of the existing SFR-CC numerical models, a common assumption is that steel fibres are uniformly distributed and randomly oriented within the matrix. However, this assumption frequently diverges from actual conditions, as the orientation and distribution of fibres are critical factors influencing the toughness of SFR-CC. Many studies have highlighted various factors affecting fibre orientation and distribution [2,56], indicating the practical challenges in achieving uniform or entirely random fibre distributions in SFR-CC specimens. It is also noted that when the orientation of a steel fibre is perpendicular to the tension direction, its contribution to the tensile strength of SFR-CC is considerably reduced, if not entirely negligible [49,51,57]. On the other hand, fibres oriented in line with the tensile stress direction prove more advantageous for elements experiencing unidirectional loading. In cementitious composite, the effectiveness of these fibres diminishes from 100 % when aligned parallel to the tensile stress, to approximately 30 % in scenarios of random distribution [1,56,58].

Recent developments have focused on enhancing the structural robustness of SFRC by utilising the superior flow characteristics of Self-Compacting Concrete (SCC). This approach aims to strategically orient the fibres in a favourable direction, achieving a more uniformly distributed arrangement [17]. Experimental studies have shown that the fibre orientation in SFR-SCC is not entirely random but tends to align parallel to the direction of bending [59,60]. Several factors influence fibre orientation in SFR-SCC, including rheological properties, formwork geometry, fibre length and type, wall effects, and casting methods [2,11,58]. These factors contribute to variations in the mechanical and fracture behaviour of SFR-SCC [61–63]. Consequently, the presumption that fibres are uniformly distributed and randomly oriented distributed might result in inaccurate predictions of the mechanical performance of structural components, particularly in the case of SFR-SCC specimens.

Zhao et al. [54] employed computational fluid dynamics as an innovative method to monitor fibre distribution within SCC, with empirical validation provided through four-point bending tests. However, a research gap still persists in understanding the overall spatial distribution of fibres [64], as well as the failure, damage, and post-peak behaviour of composite materials. Current research predominantly focuses on predicting fibre orientation and assessing the mechanical properties of SFR-SCC, often assuming random orientation in numerical simulations. However, there is lack of comprehensive analysis concerning fibre orientation, and residual tensile strength, along with the associated damage and fracture behaviours. This gap is significant because, when designing a concrete structural element reinforced with steel fibres, the most crucial factor to consider is its residual tensile strength or post-peak parameters and toughness [3,53,61–63]. A more detailed investigation of these aspects could significantly enhance the understanding of how fibre orientation affects the mechanical properties and post-cracking performance of SFR-SCC.

Hence, this study introduces a straightforward and practical discrete finite element modelling approach, designed to accurately simulate the flexural properties and post-cracking performance of SFR-SCC by incorporating various steel fibre orientations. The concrete matrix is modelled using concrete damage plasticity model in ABAQUS and is discretised into solid elements. An automated method governs the distribution and orientation of steel fibres within the matrix, ensuring confinement within the boundary of the specimen. The investigation explores three specific fibre orientations: 1) based on the flow of SCC [1], 2) random, and 3) aligned longitudinally along the length of the prism.

2. Experimental procedure

2.1. Materials and mix design

In this study, cementitious materials were employed, including Portland cement (Type 1) and ground granulated blast furnace slag (GGBS). Table 1 presents the chemical composition and physical properties of both the cement and GGBS. A superplasticizer (SP), specifically the polycarboxylate ether polymer MasterGlenium ACE 499 with a specific gravity of 1.07, was introduced. The aggregates used in this study comprised crushed limestone coarse aggregate (CA) with a maximum gravel size of 10 mm and a specific gravity of 2.65. The fine aggregate (FA) was sourced from natural river sand with a maximum particle size of 2 mm and a specific gravity of 2.55. Approximately 30 % of the natural river sand was replaced with a coarser fraction of limestone dust, also known as crushed rock sand, featuring a specific gravity of 2.6 and particle sizes ranging from 2.0 mm to 0.125 mm. This substitution of natural river sand with a coarser fraction of limestone offers potential cost savings, environmental benefits, and improved concrete durability [65–67]. Fig. 1 illustrates the particle size distribution curves for both the fine and coarse aggregates. For reinforcement, 30 mm long hooked-end steel fibres with diameters of 0.55 mm and tensile strengths of 1345 MPa were utilized in this study. Two series of high-strength SCC mixes were designed using the mix design approach outlined in [67,68]. These mixes were targeted to achieve a compressive strength of 70 MPa with a water-to-cementitious materials ratio (w/cm) of 0.40. The specific details and relative proportions of the mixes can be found in Table 2.

2.2. Specimen preparation

Effective dispersion of steel fibres in the specimens was essential, and this was achieved through a careful mixing process. In preparing the mixes described in Table 2, a structured approach was followed using a forced action pan mixer. The sequence began by blending the coarsest material, CA, with the finest, cement. This was followed by the addition of the next coarsest component FA, and GGBS, and so on. The mixing of each ingredient lasted approximately two minutes before the addition of the next. To enhance the fluidity of the mix, two-thirds of the SP was first mixed with water. This water-SP combination was then slowly merged with the dry materials and mixed for about four minutes. The final third of the SP was introduced and mixed for two minutes. At the last stage, steel fibres were gradually added into the blend and mixed thoroughly for around four minutes to ensure even distribution.

Although BS EN 14651 [69] and RILEM TC 162 [6] recommend initiating concrete pouring at the centre of the mould, several studies [11,70,71] advocate for pouring from one end in the case of SFR-SCC. Alberti et al. [18] also noted that central pouring might reduce fibre dispersion in such concrete types. Based on these insights, this study opted for an end pouring approach for all moulds. Each mixture, as specified in Table 2, was used to cast four prisms (100 mm × 100 mm × 500 mm length) and eight cubes (100 mm × 100 mm × 100 mm), and three cylinders (100 mm diameter × 200 mm length). Post-casting, the specimens were stored under standard laboratory conditions for one day, then de-moulded and submerged in water for curing at a consistent temperature of 20 (± 1) °C for a duration of 28 days.

Table 1
physical properties and chemical composition of cement and GGBS.

Composition	Cement	GGBS
SiO_2 (%)	19.69	34.34
MgO (%)	2.17	7.70
Al_2O_3 (%)	4.32	12.25
CaO (%)	63.04	39.90
Fe_2O_3 (%)	2.85	0.32
SO_3 (%)	3.12	0.23
Specific gravity	3.15	2.40
Initial Setting Time (mins)	158	-
Fineness (m^2/kg)	384	426
Loss on ignition (%)	3.03	0.34

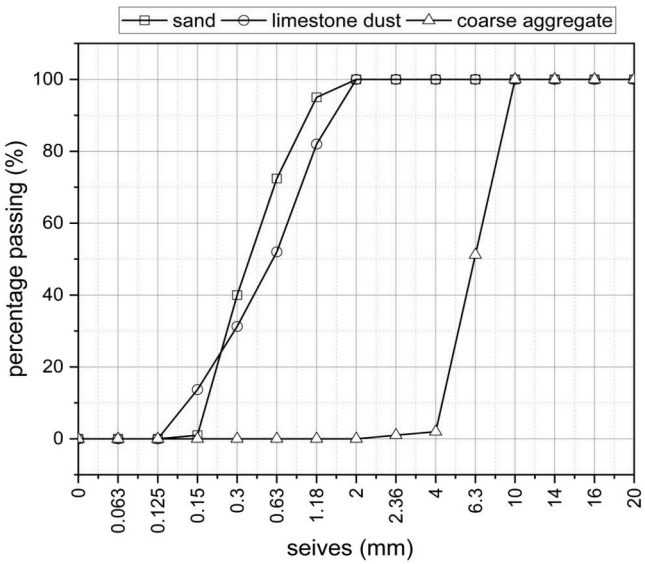

Fig. 1. Particle size distribution curves for fine and coarse aggregate.

Table 2
Mix proportions of SCC mixes, (kg/m^3).

Mix designation	Water	Cement	GGBS	SP	FA	CA	Fibre
SCC	205.6	308.4	205.6	2.3	739	796	-
SFR-SCC	205.6	308.4	205.6	3	726	796	39

2.3. Test set-up and procedure

The mixes were evaluated in their fresh state through slump flow tests (to assess flowability) and J-ring tests (to evaluate passing ability), adhering to the guidelines specified in references [72] and [73], respectively. These assessments were essential to verify the self-compaction capabilities of each mix. Cube compressive strength was measured in accordance with BS EN 12390–3 [74]. The measurement of elastic modulus (E) was conducted as per the guidelines in BS EN 12390–13 [75], involving the gradual application of load on a cylindrical specimen until it reached approximately one-third of its failure load. The resultant strain was measured using a 30 mm strain gauge.

The flexural performance and post peak behaviour of SFR-SCC was determined through a three-point bending test on notched beams, adhering to the methodology specified by RILEM and ASTM C1609 [76,77]. The beam mould dimensions for this study were chosen based on the Japan Concrete Institute Standard (JCI-S-002–2003) [78], which mandate a minimum side length of 100 mm for the beam cross-section when fibres are 40 mm or shorter. Furthermore, to comply with ASTM C1609 [77] guidelines, the mould's width was set to be at least triple the length of the fibres used. The beams were notched at the mid-span to a depth of 30 mm using a diamond saw, in accordance with JCI standards, which specify that the notch depth (a_0) should be 30 % of the beam depth and the notch width (n_0) should not exceed 5 mm. The experimental procedure involved measuring the mid-span deflection (δ) and the crack mouth opening displacement (CMOD) of each specimen. This was achieved using a Linear Variable Differential Transformer (LVDT) and a clip gauge attached to the knife edges on the specimens, facilitating the recording of both the load-deflection and load-CMOD curves. Fig. 2 provides a schematic representation of the three-point bending

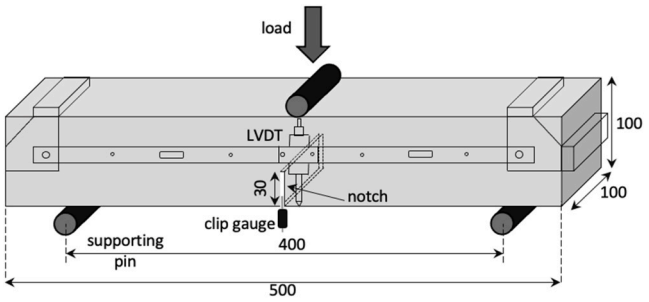

Fig. 2. Schematic representation of the three-point bending test setup.

test setup used on the notched beams.

In this study, the post-peak parameters of SFR-SCC beams are described using the first peak load (P_1), peak load (Pp), and residual loads (P^D_{600}) and (P^D_{150}) at deflections (δ) of L/600 and L/150, corresponding to deflections of 0.667 mm and 2.667 mm, respectively, following ASTM standards [77]. Additionally, the toughness (T_{150}) is described by the area under the load-versus-deflection curve up to L/150. Furthermore, the RILEM TC162-TDF recommendation [6] provides alternative method for analysing post-peak behaviour parameters to characterise the performance of concrete reinforced with steel fibres. This method measures the residual flexural tensile strength corresponding to the residual load at each CMOD of 0.5, 1.5, 2.5, and 3.5 mm.

3. Finite element simulation for SFR-SCC

3.1. Concrete modelling

The modelling of the nonlinear behaviour of concrete matrix is implemented using the concrete damaged plasticity (CDP) model in ABAQUS, which was initially proposed by Lubliner et al. [79] and subsequently refined by Lee and Fenves [80]. The CDP model utilises continuum plasticity theory to represent damage [79–81]. It incorporates the principle of isotropic damaged elasticity along with isotropic plasticity in both tension and compression. This approach enables the CDP model to accurately represent the nonlinear deformation and irreversible damage in concrete across various structural types under different loading conditions [44,82,83].

The implementation of the Concrete Damaged Plasticity (CDP) model necessitates accurate characterisation of the uniaxial compressive and tensile behaviours of concrete. To this end, the stress-strain relationship for uniaxial compression is derived in accordance with the guidelines provided in both Model Code 1990 [84] and Model Code 2010[8] (see Fig. 3). It is important to highlight that the Model Code 1990 is utilised to describe the descending branch of the stress-strain curve, particularly for strains exceeding the ultimate strain of concrete, denoted as $\varepsilon_{c,lim}$. The Model Code for concrete in compression is widely recognised for its straightforwardness and effectiveness in capturing the nonlinear behaviour of concrete. The compression behaviour of the concrete is delineated according to the following formulae.

$$\sigma_c = f_c\left[k\frac{\varepsilon_c}{\varepsilon_{c1}} - \left(\frac{\varepsilon_c}{\varepsilon_{c1}}\right)^2\right] \Big/ \left[1+(k-2)\frac{\varepsilon_c}{\varepsilon_{c1}}\right] \text{for} 0 < \varepsilon_c < \varepsilon_{c,lim} \quad (1)$$

$$\sigma_c = f_c\left[\left(\frac{1}{e}\xi - \frac{2}{e^2}\right)\left(\frac{\varepsilon_c}{\varepsilon_{c1}}\right)^2 + \left(\frac{4}{e} - \xi\right)\frac{\varepsilon_c}{\varepsilon_{c1}}\right]^{-1} \text{for} \varepsilon_c > \varepsilon_{c,lim} \quad (2)$$

Where

$$k = E_{ci}/E_{c1} \quad (3)$$

$$e = \varepsilon_{c,lim}/\varepsilon_{c1} \quad (4)$$

$$\xi = 4\frac{[e^2(k-2)+2e-k]}{[e(k-2)+1]^2} \quad (5)$$

$$\varepsilon_{c,lim} = \varepsilon_{c1}\left[\frac{1}{2}\left(\frac{k}{2}+1\right) + \sqrt{\frac{1}{4}\left(\frac{k}{2}+1\right)^2 - \frac{1}{2}}\right] \quad (6)$$

Where E_{ci}, denoting the initial tangent modulus, is equivalent to E_c. The term E_{c1}, defined as f_c/ε_{c1}, signifies the secant modulus extending from the origin to the maximum compressive stress (f_c). The strain at peak compressive stress, ε_{c1}, is calculated as follows [85,86]

$$\varepsilon_{c1} = 1.60(f_c/10)^{0.25} \Big/ 1000 \quad (7)$$

The compression damage variable (d_c), which is shown in Fig. 3, can be expressed as outlined in [79,81,87]

$$d_c = 1 - (\sigma_c/f_c) \quad (8)$$

The tensile behaviour of concrete is initially characterised by a linear elastic stress-strain relationship until its tensile strength is reached. Beyond this point, crack formation leads to a decrease in stress via a softening process, which proceeds until the material ultimately loses tensile strength. Various models, such as linear, bilinear, or exponential, can describe the relationship between stress and crack displacement [88]. This study employs an exponential model to define the post-peak softening phase, as proposed by Hordijk [89], to detail the decreasing stress in relation to crack width. This relationship is graphically represented in and is determined by two key parameters: the tensile strength (f_{ct}) and the fracture energy (G_f). The relationship between tensile stress

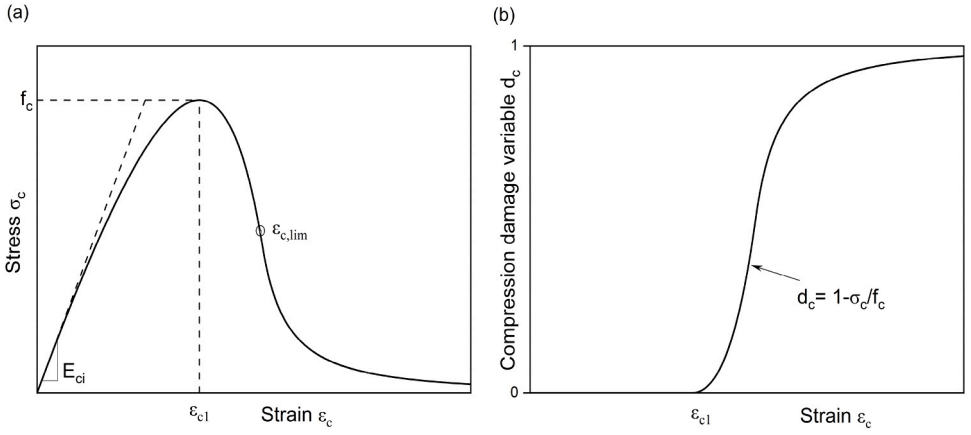

Fig. 3. Constitutive models for concrete under compression: (a) stress-strain relationship, (b) compression damage parameter.

and crack width, as formulated by Hordijk [89], is defined by the following mathematical expressions.

$$\frac{\sigma_t}{f_{ct}} = \left[1 + \left(c_1 \frac{w}{w_{cr}}\right)^3\right] e^{-c_2 \frac{w}{w_{cr}}} - \frac{w}{w_{cr}}\left(1 + c_1^3\right) e^{-c_2} \quad (9)$$

$$w_{cr} = 5.136 \frac{G_f}{f_{ct}} \quad (10)$$

Where c_1 and c_2 equal to 3 and 6.93 respectively.

The stress-displacement relationship presented in Eq. (9) is transformed into a stress-strain relationship through the application of crack band theory [90]. This transformation is achieved by dividing the crack displacement by the characteristic crack length of the elements, thereby addressing issues related to fracture localization and mesh sensitivity [88,91–93]. Within the framework of 3D elements, the characteristic length is determined as the cubic root of the volume of the element. For the simulations detailed in this study, the chosen critical length was established as 5 mm, matching the notch length of the beam.

The fracture energy quantifies the energy required to propagate a tensile crack over a unit area [91]. The tensile strength and fracture energy are predicted from the formulae given in the JSCE design code [9].

$$f_{ct} = 0.23 \quad (f_c)^{2/3} \quad (11)$$

$$G_f = 10 \quad (d_{max})^{0.33} (f_c)^{0.33} \quad (12)$$

Where d_{max} is the maximum aggregate size (in mm). The tension damage variable (d_t), as seen in Fig. 4, was defined as suggested by Lubliner et al. [79,87,94]

$$d_t = 1 - (\sigma_t / f_{ct}) \quad (13)$$

Furthermore, the definition of the CDP model in ABAQUS also requires the input of five key parameters: the dilation angle φ (expressed in degree), flow potential eccentricity $\in$, the ratio of initial biaxial to uniaxial compressive yield stress σ_{b0}/σ_{c0}, the ratio of the second stress invariant between tensile and compressive meridians K, and the viscosity parameter μ. In the simulations conducted for this study, these parameters are consistently set to 31 degrees, 0.1, 1.16, 0.667, and 0.005, in the respective order [37].

3.2. Fibre structure modelling

3.2.1. Fibre distribution and orientation

The flowchart illustrating the generation of fibre distribution using MATLAB software is depicted in Fig. 5. The total number of steel fibres within the specimen was calculated based on the assumed fibre volume fraction and the geometry of the specimen. The total fibre volume in the specimen was determined using the steel fibre volume fraction and the total volume of specimen. This value was then divided by the volume of a single fibre, calculated from its length and cross-sectional area, to estimate the total number of fibres. The distribution of each individual fibre is represented by angles α and β, with α ranging from 0 to 90° and β from 0 to 360°, along with the coordinates of both fibre ends as shown in Fig. 6. Each fibre must be positioned so that the body of the fibre does not fall within the region of notch or extend outside the boundaries of the specimen.

In the finite element model, the fibre structure within the concrete composite is generated based on different scenarios of fibre orientation to deepen the understanding of its impact on the post-peak behaviour of concrete. The first scenario features controlled fibre orientations, specifically designed to mimic the alignment of steel fibre found in SCC. These scenarios ensure that the majority of fibres align with the flow direction, a setup corroborated by previous research [1] and illustrated in Fig. 7.

In contrast, the second scenario introduces a random orientation, reflecting the typical alignment of steel fibres in normally vibrated concrete. Experimental studies confirm this randomness [16,17], which is influenced by factors such as mechanical vibration during compaction, placement methods, configurations of boundary forms, and the properties of the steel fibres during the production process in SFRC. The visual representation of this orientation is detailed in Fig. 8.

Moreover, an important exploration is conducted on a scenario where all fibres are precisely horizontally, perpendicular to the direction of the applied vertical load. This particular orientation is studied to assess its potential in maximising flexural strength, toughness, and overall post-peak behaviour. Each orientation scenario is supported by four distinct distribution models, ensuring a comprehensive and uniform dispersion of fibres. Table 3 summarises the statistical characteristics of these fibre orientations within the concrete matrix.

3.2.2. Constitutive model for the steel fibre

The formulation of the embedded fibre model used in this study incorporates the bond-slip behaviour indirectly. Therefore, the embedded elements are modelled with an assumption of perfect bonding to avoid conformal meshes. In fact, the bond-slip behaviour for a single fibre at various inclination angles is indirectly simulated by transforming a load-slip relationship ($P - s$) into a tensile stress-strain relation (σ_f–ε_f). The constitutive law for the steel fibres is formulated from their pull-out response. Thus, the stress σ_f in the fibres is determined by the ratio of the pull-out force P to the cross-sectional area of the fibre as shown in Eq. (14) (where d_f is the fibre diameter). Similarly, the strain ε_f in the fibres is derived from the ratio of the slip length s to the fibre's length l_f. Eqs. (14) and (15) are used to calculate the stress σ_f and strain ε_f in the fibre, respectively.

$$\sigma_f = \frac{P}{\pi d_f^2 / 4} \quad (14)$$

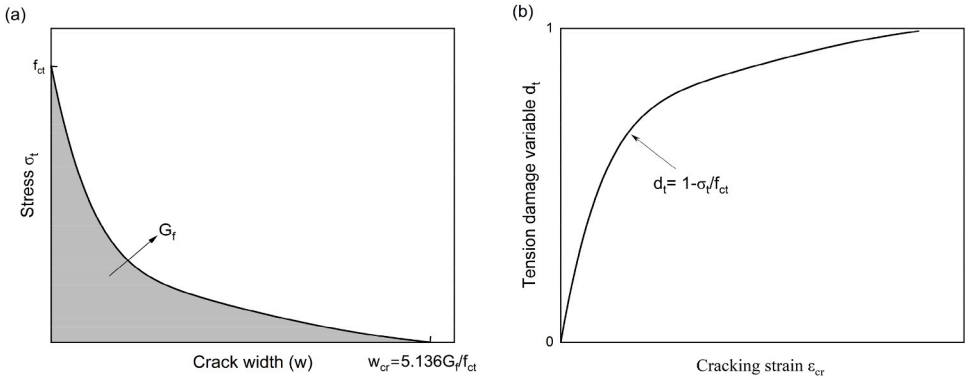

Fig. 4. Constitutive models of concrete in tension: (a) stress-crack width relationship, (b) tensile damage parameter.

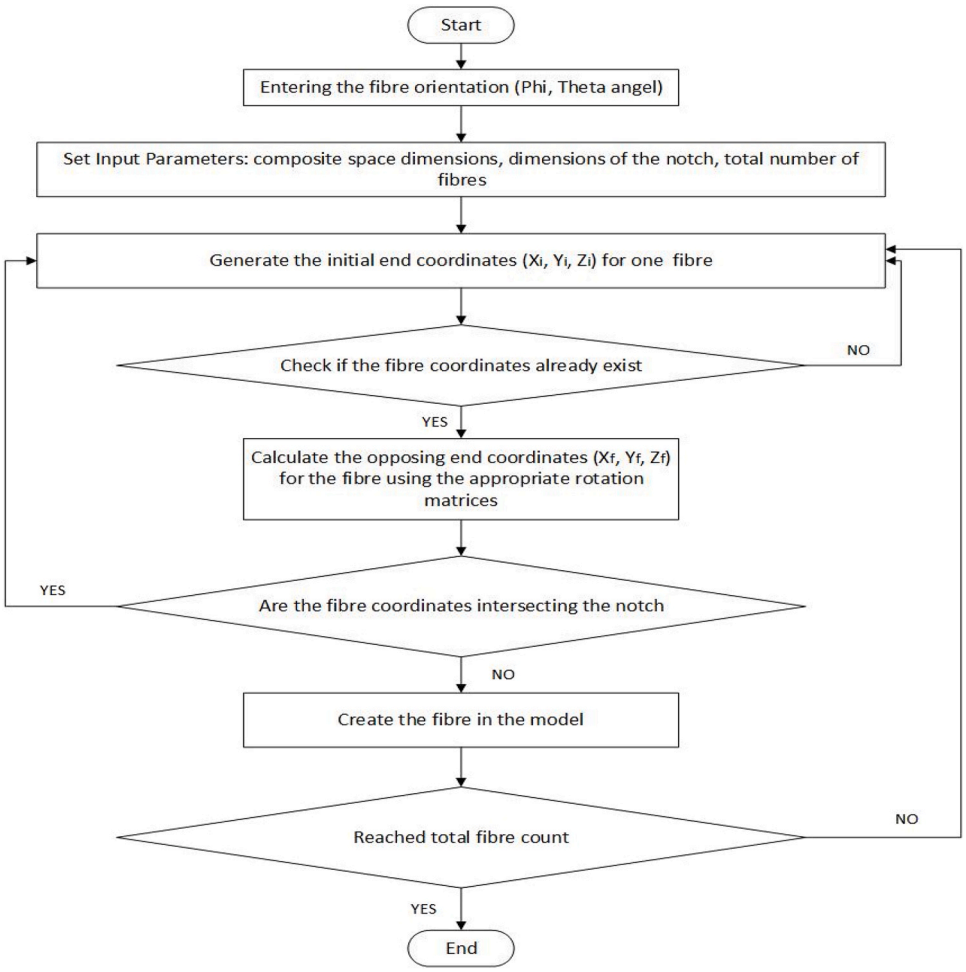

Fig. 5. Flowchart outlining the process for simulating steel fibre distribution in SCC matrix.

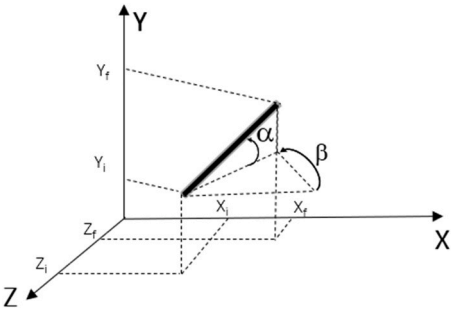

Fig. 6. Fibre orientation and coordination in three dimensions.

$$\varepsilon_f = \frac{s}{l_f} \tag{15}$$

In the experimental analysis, the pull-out response of steel fibres is characterised by the relationship between the pull-out force and the slip length. When this pull-out force-slip length relationship is translated into a stress-strain relationship, the length in Eq. (15) is not necessarily the physical length of the fibre but rather equivalent to a simulated length that yields the accurate slip length s under the same force P. In the finite element models developed by Abrishambaf et al. [95] and Cunha et al. [49,50] where each fibre is segmented into multiple short fibres by the solid elements representing the concrete matrix, this simulated length is equivalent to the crack band width. Conversely, in the models by Zhao et al. [54],Pros et al. [55] and Yu et al. [51] where fibres are directly embedded within the plain concrete matrix, the simulated length corresponds to the real fibre length. In the current study, the steel fibres are also directly embedded in the concrete matrix, thus aligns with fibre treatment approach adopted by Zhao et al. [54], Pros et al. [55] and Yu et al. [51]

3.2.3. *Pull-out response of the steel fibres*

The inclination angles of fibres significantly influence their pull-out behaviour, resulting in a range of pull-out responses. This variability in fibre orientation within the concrete matrix necessitates the use of an analytical method to evaluate the pull-out response across different inclination angles. Hooked fibres display the same characteristics seen in inclined straight fibres, such as fibre debonding, matrix spalling, frictional sliding, and fibre extraction. Moreover, the hooked ends cause plastic deformations, which require an increased force for pull-out, thereby exacerbating the matrix spalling effects in inclined fibres. In response to these observations, Laranjeira et al. [28,29] have developed an analytical model to simulate the behaviour of inclined steel fibres with hooked ends, a method adopted in this study. This model considers essential input variables, such as the material properties and the pull-out behaviour of aligned fibres under load. For a comprehensive description of the analytical model, including the detailed derivations of the equations and definitions of all symbols, readers are encouraged to consult the original works by Laranjeira et al. [28,29]. It generates a pull-out diagram for inclined hooked steel fibres, depicted in Fig. 9 and characterised by eight key points, detailed in Table 4 for convenience. Each point represents a distinct stage in the pull-out process of inclined fibres. The model primarily addresses steel fibres with lengths of 30–60 mm

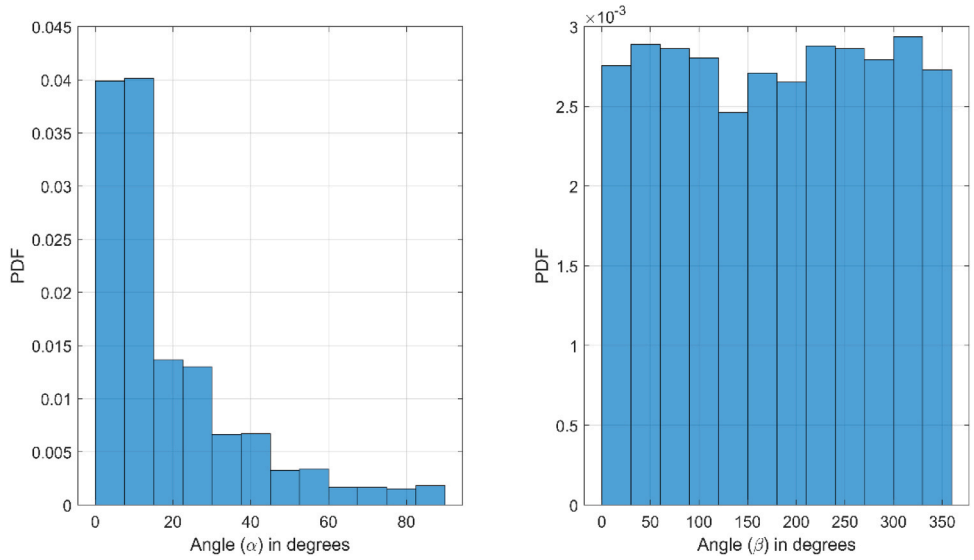

Fig. 7. Histogram of controlled fibre alignments in SCC, showing predominant flow direction orientation. PDF refers to the Probability Density Function, representing the distribution of fibre orientations in terms of angle α.

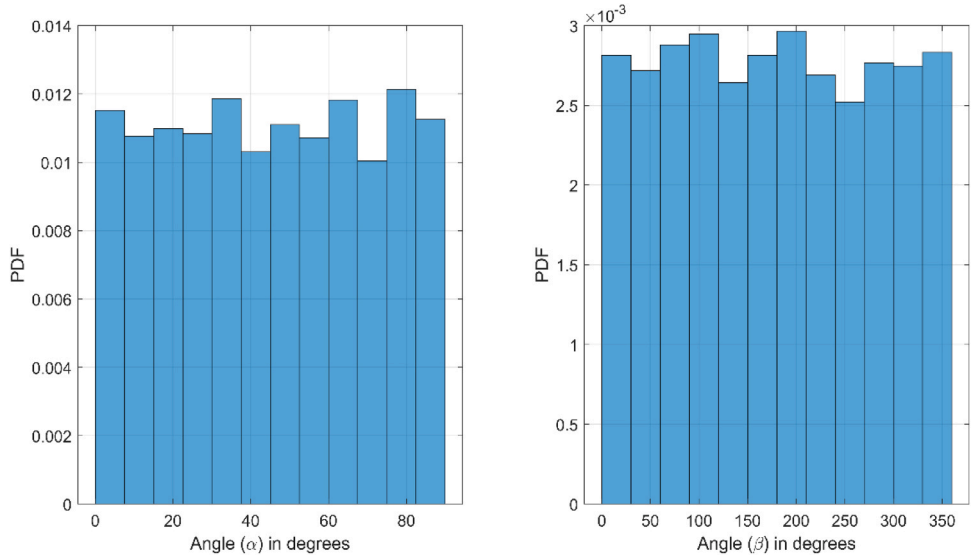

Fig. 8. Distribution of random fibre orientations. PDF refers to the Probability Density Function, representing the distribution of fibre orientations in terms of angle α.

Table 3
Statistical summary of fibre orientation angles α and β for three scenarios in SCC matrix.

Scenario	Angles	Mean	Standard Deviation	25 %	Median	75 %
Flow-based orientation	α	19.2	18.9	6.2	12.4	26.6
	β	180.4	104.4	88.7	182.2	271.3
Random orientation	α	44.9	26.1	23.0	45.0	68.0
	β	178.7	104.2	89.0	178.0	270.0

and diameters between 0.5 and 1.0 mm, set within cementitious matrices with compressive strengths not exceeding 90 MPa.

3.3. Numerical simulation models setup

The plain SCC matrix is modelled using the CDP, as presented in Section 3.1. The parameters adopted, along with the compressive strength and elastic modulus obtained from the experimental results, are detailed in Table 5. Additionally, the matrix is modelled using three-dimensional, eight-node continuum elements with reduced integration points (C3D8R). On the other hand, steel fibres are represented using three-dimensional, two-node truss elements (T3D2). All numerical models in this study were tested at a loading rate of 0.005 mm/s.

The placement of steel fibres within the concrete matrix, as exemplified by Fig. 10, is produced using a Python script. This script is fully integrated into ABAQUS software, facilitating the automatic generation and accurate positioning of steel fibres in accordance with their predefined designated locations and orientations. This careful placement ensures the fibres neither impinge upon the notch area nor extend beyond the boundaries of the specimen.

Owing to the complexity of defining a unique ε_f-σ_f law for every possible fibre inclination, laws corresponding to fibre orientation angles of 7.5°, 22.5°, 37.5°, 52.5°, and 67.5° were applied to truss elements within the orientation angle ranges of [0°, 15°], [15°, 30°], [30°, 45°], [45°, 60°], and [60°, 75°], respectively. Fibres positioned at an

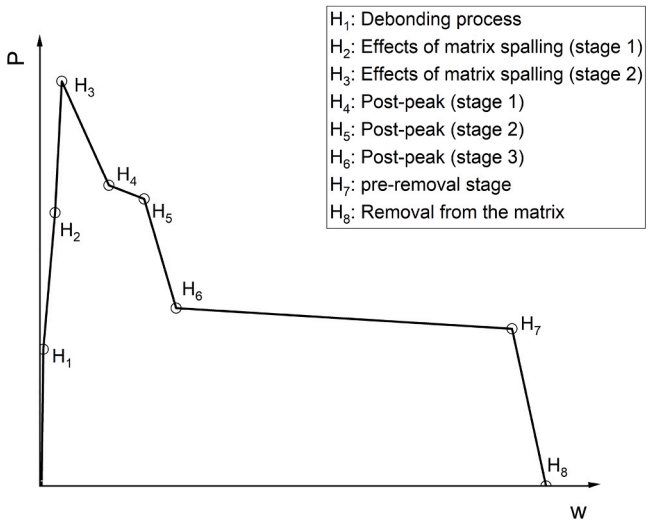

Fig. 9. Schematic diagram of the pull-out response for an inclined hooked-end fibre, adapted from [28].

Table 4
Summary of formulations defining the analytical model for hooked-end fibre pull-out as proposed by Laranjeira et al. [28].

Points	Equation
H_1	$P_{H1} = P_{S1} = P_{S01}\cos\theta \quad w_{H1} = w_{S1} = w_{S01}$
H_2	$P_{H2} = \left(P_{SO11}L_{eff(H2)} + \Delta P_{H01}\frac{L_e - 6\times L_{SPH1}}{L_e}\right)\cos + \mu P_{S01}\sin\theta\cos\frac{\theta}{2} \quad w_{H2} = w_{H1} + \Delta w_{H01}\cos\theta\frac{L_e - 6\times L_{SP1}}{L_e} + \Delta w_{SP1}$
H_3	$P_{H3} = \left(P_{SO1}L_{eff(H3)} + \Delta P_{HO1}\right)\cos\theta + \mu P_{H01}\sin\theta\cos\frac{\theta}{2} \quad w_{H3} = w_{H1} + \Delta w_{H01}\cos\theta + \Delta w_{SP1} + \Delta w_{SP2}$
H_4	$P_{H4} = \left(P_{S01}L_{eff\ (H4)} + \sum_{i=1}^{2}\Delta P_{H0i}\right)\cos\theta + \mu P_{H01}\sin\theta\cos\frac{\theta}{2} \quad w_{H4} = w_{H3} + \Delta w_{H02}\cos\theta$
H_5	$P_{H5} = \left(P_{S01}L_{eff(H5)} + \sum_{i=1}^{3}\Delta P_{H0i}\right)\cos\theta + \mu P_{H01}\sin\theta\cos\frac{\theta}{2} \quad w_{H5} = w_{H4} + \Delta w_{H03}\cos\theta$
H_6	$P_{H6} = \left(P_{SO2}L_{eff(H6)} + \sum_{i=1}^{4}\Delta P_{HOi}\right)\cos\theta + \mu P_{H01}\sin\theta\cos\frac{\theta}{2} \quad w_{H6} = w_{H5} + \Delta w_{H04}\cos\theta$
H_7	$P_{H7} = \left(\sum_{i=1}^{4}\Delta P_{H0i}\right)\cos\theta + \mu P_{H01}\sin\theta\cos\frac{\theta}{2} \quad w_{H7} = L_e - (L_{SP1} + L_{SP2} + L_{H,crit})$
H_8	$P_{H8} = 0 \quad w_{H8} = L_e - (L_{SP1} + L_{SP2})$

Table 5
Properties of plain SCC used in the numerical simulation.

Property	Value
Compressive strength (f_c)	71.7 N/mm^2
Young's modulus (E)	41,060 N/mm^2
Poisson's ratio (ν)	0.2
Tensile strength ($f_{c\ t}$)	3.97 N/mm^2
Fracture energy (G_f)	0.0876 N/mm
Crack band-width (l_b)	5 mm

inclination greater than 75° were assumed to exhibit no slippage, as indicated in references [37,54,95]. In this numerical simulation, the behaviour of hooked-end fibres was investigated by identifying eight critical points, from (σ_{f1}–ε_{f1}) to (σ_{f8}–ε_{f8}). Due to the similarities in the compressive strength of the concrete matrix and the properties of the hooked fibres, as detailed in reference [95], the values for the maximum pull-out force and the corresponding slip are sourced from this reference. The other parameters are consistent with those listed in [28,54]. Table 6 provides a comprehensive description of the input parameters used for these calculations of the analytical model for pull-out response of different inclinations of hooked-end steel fibres. Fig. 11 illustrates the pull-out behaviour of the fibres at various fibre orientation angles 7.5°, 22.5°, 37.5°, 52.5°, and 67.5° using an analytical model based on the approach proposed by Laranjeira et al.[28]. The ε_f-σ_f laws for these specific fibre orientation angles were derived and are detailed in Fig. 12.

4. Results and discussion

4.1. Experimental results

This section presents the results of the experimental program detailed in Section 2, along with numerical simulations of three-point bending tests. These simulations aim to assess the effectiveness of numerical method in determining the post-cracking parameters of SFR-SCC, considering varied fibre orientations and distributions.

Table 7 presents the results of the slump flow and J-ring tests. All tested mixes showed no signs of bleeding or segregation upon detailed visual inspection. Compressive strength, unit weight, and elastic modulus measurements for the specimens are detailed in Table 8. Furthermore, the findings from the three-point bending tests on notched prisms will be compared with the results of the numerical simulations for a thorough analysis.

4.2. Comparison of experimental and numerical simulation results of plain SCC

The recorded load-deflection diagram obtained from the experimental investigation on notched beams using a three-point bending test, along with numerical simulation results, is shown in Fig. 13. The experimental envelope illustrates the variability in the data, indicating that while there is some scatter, the majority of the experimental results fall within a certain range around the average curve. The experimental envelope represents the maximum and minimum bounds of the data collected from four test specimens. The numerical simulation in this paper employs the CDP model described previously, utilising the elastic and compressive strength values obtained from the experiments, while predicting the tensile strength and fracture energy values according to the JSCE design code [9]. The simulation results of the load-deflection closely follow the average experimental curve, demonstrating a high degree of accuracy. In addition, Fig. 14 presents the load-CMOD diagram of experimental and simulation results, showing that the numerical simulation results closely match the experimental outcomes. Table 9 shows the peak load, deflection at peak load, CMOD at peak load, and area under the load-deflection curve of plain SCC, along with the error between experimental and numerical simulation results. It can be seen that the experimental results are very close to the numerical results. This close agreement between the experimental data and the simulation validates the accuracy of the computational model in predicting the flexural and damage behaviour of SCC. The comparison between experimental and simulation results is an important step before investigating the flexural and post-peak behaviour of SFR-SCC by experimental and simulation methods.

4.3. Comparison of experimental and numerical simulation results of SFR-SCC

Steel fibres are widely recognised as most effective after the cracking of a brittle cementitious matrix [3]. Consequently, accurately simulating flexural strength and the post-cracking parameters of steel fibre composite is crucial for enhancing the understanding and application of this composite material. This, in turn, can facilitate its widespread adoption in the construction industry. The flexural behaviour of cementitious composites reinforced with fibres can be classified into deflection-softening and deflection-hardening types. This classification is important for determining the appropriateness of the materials for various structural applications. Deflection-hardening composites exhibit

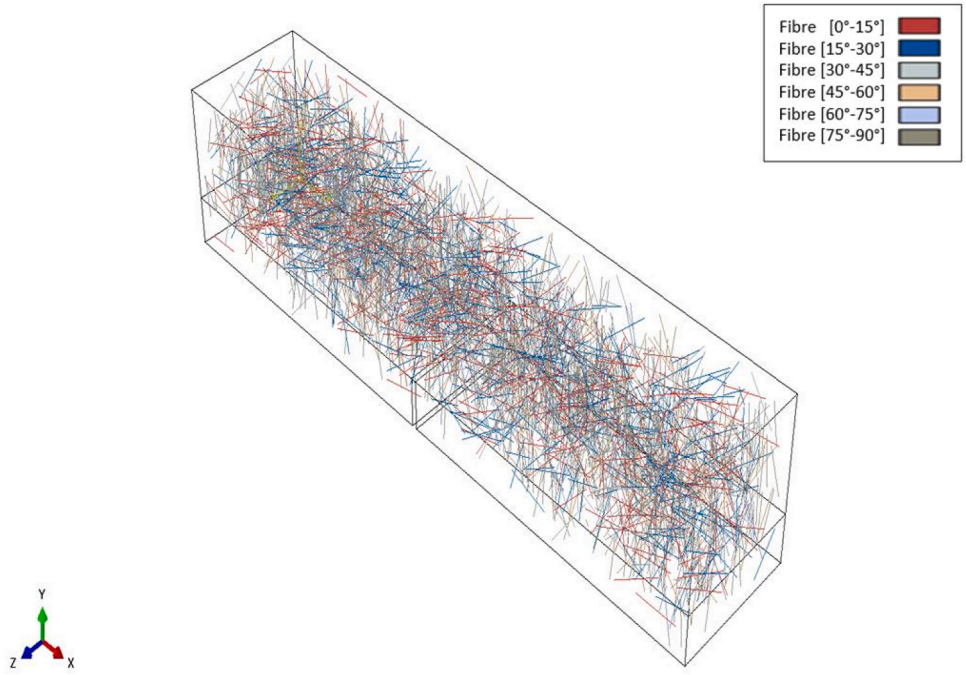

Fig. 10. Example of position of steel fibres within a concrete matrix (random orientation) in the numerical model.

Table 6
Input parameters for analytical model of pull-out response.

L_e (mm)	15	P_{SO1} (N)	105	P_{H02} (N)	182
d (mm)	0.55	W_{S01} (mm)	0.035	W_{H02} (mm)	2.2
σ_u (N/mm^2)	1345	P_{SO2} (N)	52.5	P_{H03} (N)	155
$f_{c\ t}$ (N/mm^2)	3.97	W_{S01} (mm)	0.3	W_{H03} (mm)	3.5
N	1	P_{H01} (N)	255	P_{H04} (N)	118
μ	0.6	W_{H01} (mm)	0.636	W_{H04} (mm)	5

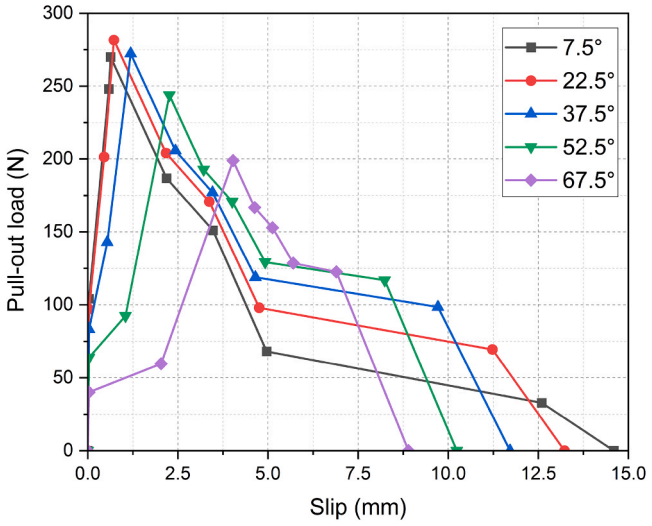

Fig. 11. Pull-out load-slip curves for hooked-end fibres at different inclinations 22.5°, 37.5°, 52.5°, and 67.5°.

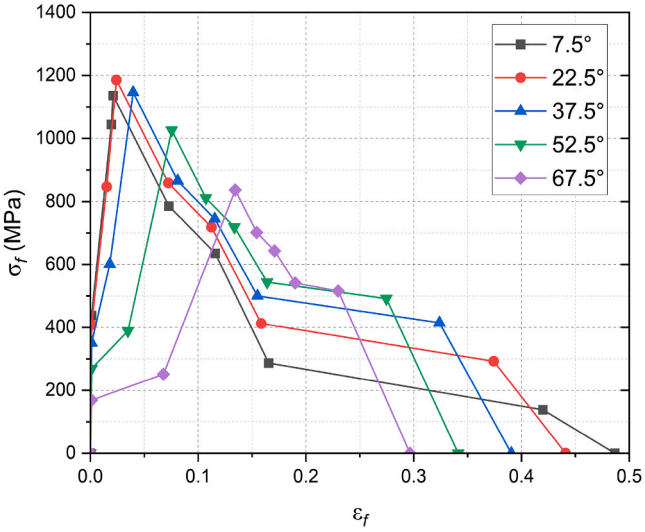

Fig. 12. Stress-strain curves for hooked end steel fibres at various inclinations.

Table 7
Results of slump flow and J-ring flow tests for SCC mixes.

Mix designation	Slump flow test		J-ring* flow test	
	Spread (mm)	t_{500} (s)	Spread (mm)	t_{500j} (s)
SCC	740	1.7	680	2
SFR-SCC	770	2	690	2.3

* J-ring apparatus with 12 steel rods

superior load-carrying capacity after initial cracking compared to both plain concrete and deflection-softening fibre-reinforced composites [96]

Fig. 15 illustrates the outcomes of three-point bending tests performed on notched beams made of SCC reinforced with steel fibres, alongside comparative simulated results that consider the fibre orientation trend based on steel fibre flow. The average experimental curve shows an initial sharp increase in load, reflecting the elastic response of the material, followed by a plateau and then a gradual decrease in load, indicating deflection-hardening behaviour. The experimental envelope highlights variability among the tested specimens, probably due to differences in number, distribution, and

Table 8
Compressive strength and elastic modulus results for mixes at 28 days.

Mix designation	Compressive strength (MPa)	Unit weight (kg/m^3)	Elastic Modulus GPa)
SCC	71.7	2398	41.06
SFR-SCC	69.2	2403	41.62

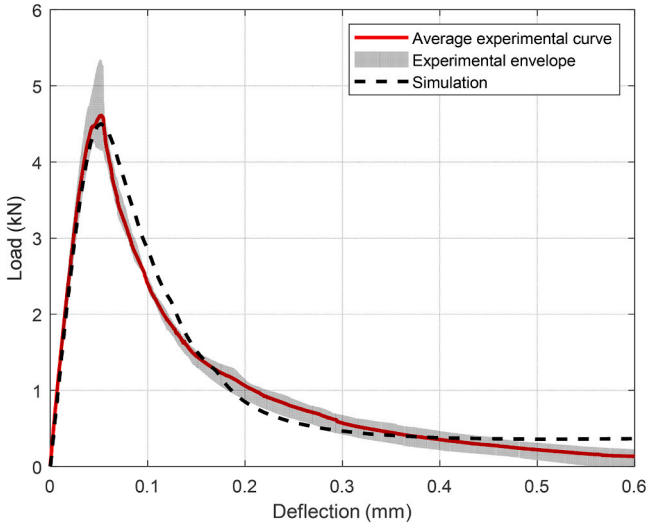

Fig. 13. Comparison of load-deflection response of plain SCC, comparing experimental data with simulation results.

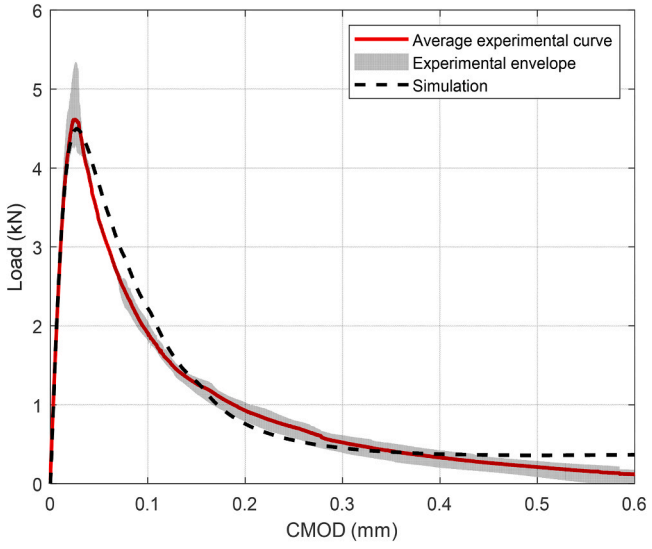

Fig. 14. Load-CMOD curves for experimental and simulation results of plain SCC.

Table 9
Comparison of experimental and numerical results for plain SCC.

	Experimental Results		Simulation	Error (%)
	Mean	CoV(%)		
Peak Load (kN)	4.7	9.3	4.5	4.2
Deflection at peak load (mm)	0.026	12.6	0.027	5.57
CMOD at peak load (mm)	0.047	15.6	0.052	9.04
Toughness kN.mm	0.654	8	0.664	1.5

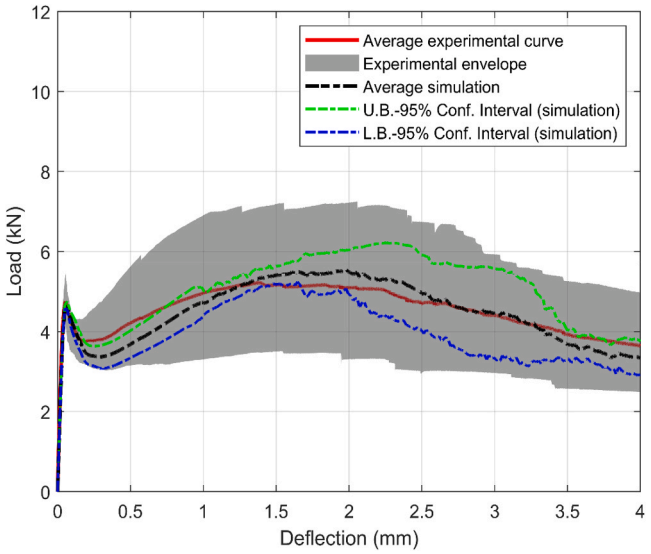

Fig. 15. Experimental and simulation (orientation based on flow) results of load-deflection curves of notched SFR-SCC beams.

orientation of fibres on the fracture surface. The average simulation curve is derived from four distributions using the same probability density function (PDF) for fibre orientation based on fibre flow in SCC. The simulated results, represented by the average of simulations along with the 95 % confidence intervals, closely align with the experimental data. Both the initial elastic response and the post-cracking load-bearing capacity are well captured by the numerical simulation approach.

In this study, the influence of steel fibre on the first peak load is slight. In plain SCC, the first peak load is approximately 4.7 kN at a deflection of 0.026 mm, while in SFR-SCC, it is around 4.85 kN at a deflection of 0.055 mm. Importantly, the numerical simulation results successfully capture this slight improvement. In the simulation of plain SCC, the first peak load is 4.5 kN at a deflection of 0.027 mm, whereas in the simulation of SFR-SCC, the first peak load is 4.66 kN at a deflection of 0.058 mm. The effect of steel fibre is more pronounced on the residual loads and toughness of the fibre-reinforced composite.

Table 10 presents the post-peak parameters of SFR-SCC derived from both experimental and numerical simulations results, including the first peak load (P_1), deflection at first peak (δ_{P_1}), peak load (Pp) deflection at (δ_{P_p}), and residual loads (P^D_{600}) and (P^D_{150}) at deflections (δ) of L/600 and L/150 following ASTM standards [77]. The post-peak loads from the numerical simulations align well with the experimental results. This demonstrates that the simulation approach can be effectively used to model larger structural members, as it accurately captures the post-cracking behaviour of SFR-SCC.

In Addition, the flexural strength and post-cracking parameter can be obtained based on the RILEM TC162-TDF recommendation [6], which measures the residual flexural tensile strength corresponding to the residual load at each CMOD of 0.5, 1.5, 2.5, and 3.5 mm. Fig. 16 shows the experimental data and numerical simulation curves of the load-CMOD diagram, which indicate that the numerical simulation curve agrees

Table 10
post-peak parameters of SFR-SCC from experimental and numerical simulations results.

	P_1 (kN)	δ_{P_1} (mm)	P_P (kN)	(δ_{P_p}), (mm)	P^D_{600} (kN)	P^D_{150} (kN)
Experimental	4.85	0.055	5.71	1.951*	4.52	4.70
Simulation	4.66	0.058	5.82	1.978	4.04	4.76
Error (%)	3.92	5.45	1.93	1.38	10.62	1.28

* This is for the only samples showing strain hardening

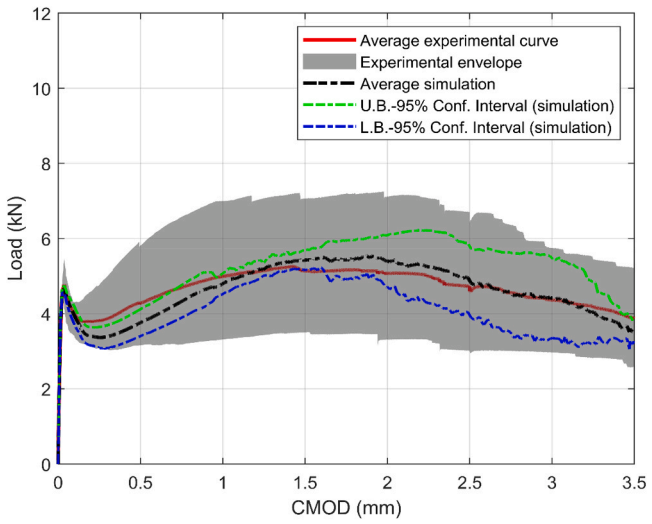

Fig. 16. Experimental and simulation (orientation based on flow) results of load-CMOD curves of notched SFR-SCC beams.

very well with the experimental data. This comparison between experimental and simulated results highlights the accuracy of this method for simulating post-cracking parameters. It also underscores the importance of accurately modelling fibre orientation within the SCC matrix as a key factor for the simulations. The strong correlation between the two data sets validates the effectiveness of the simulation approach. These findings reinforce the well-established significance of fibre orientation in influencing the mechanical and post-peak performance of SFR-SCC, while providing additional quantitative insights into the effects of specific fibre orientation.

The finite element analysis detailed in this study provides insights into the structural integrity and damage progression of a modelled beam under various loading stages. The numerical simulation model is proficient at monitoring damage initiation, stress, and strain in the concrete. Additionally, the explicit representation of steel fibres facilitates the observation of mechanical properties such as axial fibre stress distribution. This setup enables the evaluation of the influence of fibre orientation and distribution on the flexural behaviour of SFR-SCC.

Fig. 17 displays the damage index (DAMAGT) at deflection of 0.01 mm and 2.667 mm. As anticipated, damage propagation in the concrete was primarily observed at the mid-spans within the notch of the beam. DAMAGET, part of the Concrete Damage Plasticity (CDP) model, is used to approximate cracking in tension zones. The CDP model predicts crack formation when the maximum principal plastic strain reaches a positive value, with cracks developing perpendicular to the direction of these strains [80,87]. However, the CDP model does not provide detailed crack data, such as crack width, as it operates on a continuum scale rather than explicitly simulating discrete cracks. It is important to note that the damage shown in Fig. 18 pertains to plain SCC, not SFR-SCC. This serves as a reference to validate the accuracy of the simulation in capturing damage progression in the correct locations, confirming the reliability of the model for further simulations involving fibre-reinforced concrete.

In addition, Fig. 18 and Fig. 19 provide additional insights into key parameters influencing the behaviour of SFR-SCC under varying loading conditions: the equivalent plastic strain (PEEQ) and axial fibre stress (S1,11), respectively. The equivalent plastic strain (PEEQ) is widely utilised to evaluate material plastic behaviour, particularly the extent of irreversible deformation it can undergo before reaching failure. In contrast, axial fibre stress (S1,11) represents the stress response along the longitudinal direction of the fibres.

At a minimal deflection of 0.01 mm (Fig. 18(a) and Fig. 19(a)), both PEEQ values and stress levels are relatively low, indicating negligible plastic deformation and a relatively uniform stress distribution across the prism. However, at a deflection of 2.667 mm (Fig. 18(b) and Fig. 19 (b)), there is a substantial increase in both PEEQ and stress, particularly concentrated in the central region above the notch. The significant rise in PEEQ highlights areas of intense plastic deformation, while the increased stress values indicate zones experiencing high tensile forces, marking critical points of potential failure. This dual increase in PEEQ and stress at higher deflections highlights critical points of potential failure. In these areas, the orientation of the steel fibres is particularly significant as it greatly influences the mechanical response and distribution of stresses and strains, thus playing a critical role in the overall structural performance and integrity of the SFR-SCC.

4.4. *Effect of random orientation of fibre*

Random orientations of steel fibres were generated in the numerical simulation to explore their impact on the flexural and post-peak parameters. Typically, the orientation of steel fibres in normally vibrated concrete is random, a phenomenon well-documented in the literature [16,17]. However, the strategic use of steel fibres in SCC aims to orient the fibres in a favourable direction, thus achieving a more uniformly distributed arrangement that enhances the mechanical properties of the

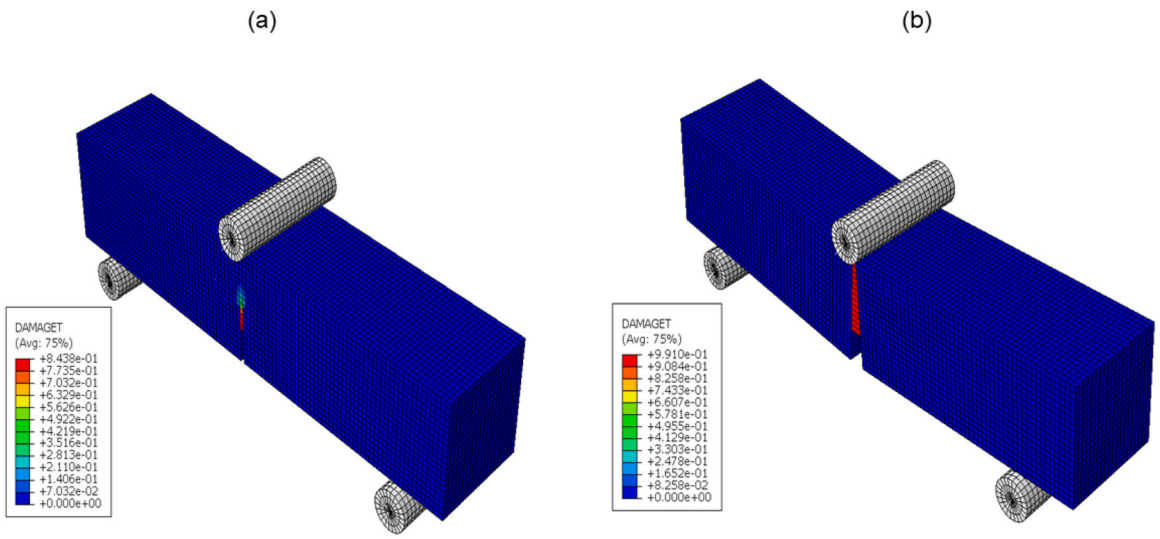

Fig. 17. Damage index DAMAGET of SCC beam at deflection of (a) 0.01 mm deflection (b) 2.667 mm (scale factor =5).

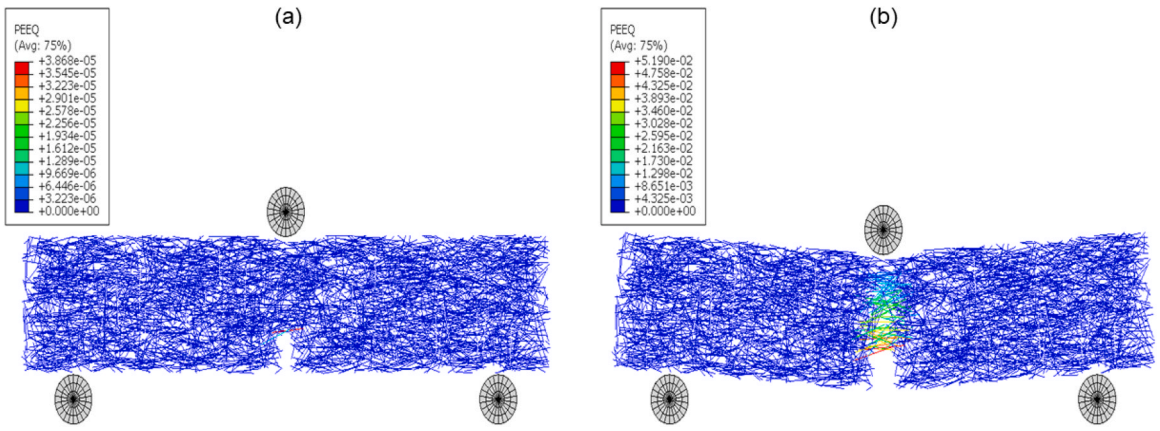

Fig. 18. Equivalent plastic strain (PEEQ) of the steel fibres at deflection of (a) 0.01 mm deflection (b) 2.667 mm (scale factor =5).

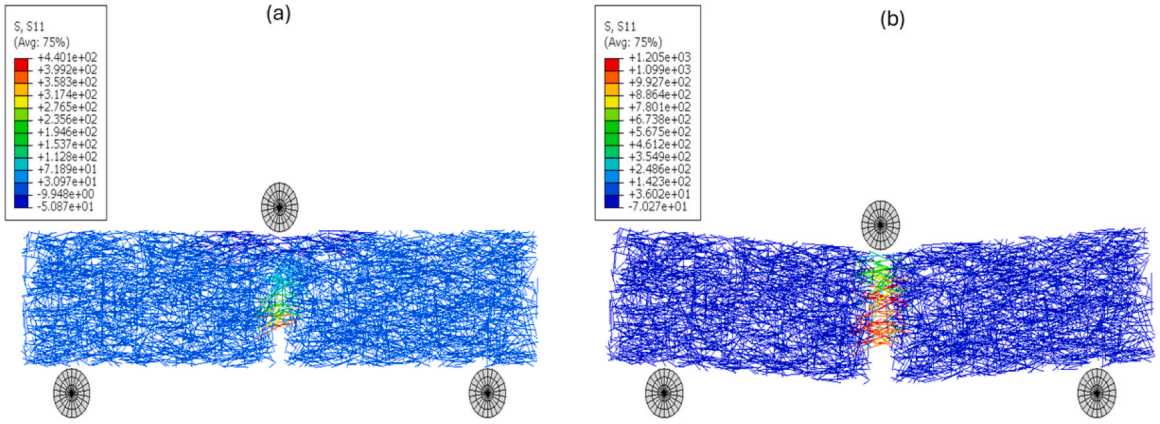

Fig. 19. Stress on fibre element at deflection of (a) 0.01 mm deflection (b) 2.667 mm (scale factor =5).

concrete [17]. This targeted alignment is intended to optimise the structural capabilities and fracture properties of the concrete matrix but is often not captured in simulations that assume random orientation of steel fibres.

Fig. 20 and Fig. 21 provide a comparative analysis between experimental results and numerical simulations, focusing on the random orientation of steel fibres, for both the load-deflection and load-CMOD

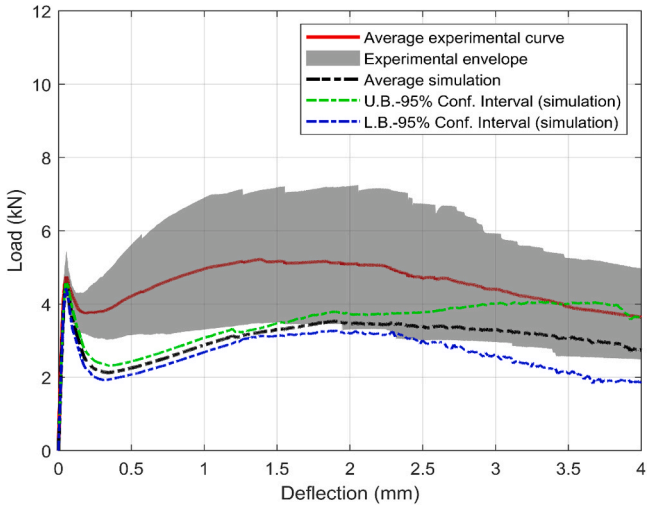

Fig. 20. Experimental and simulation (random orientation) results of load-deflection curves of notched SFR-SCC beams.

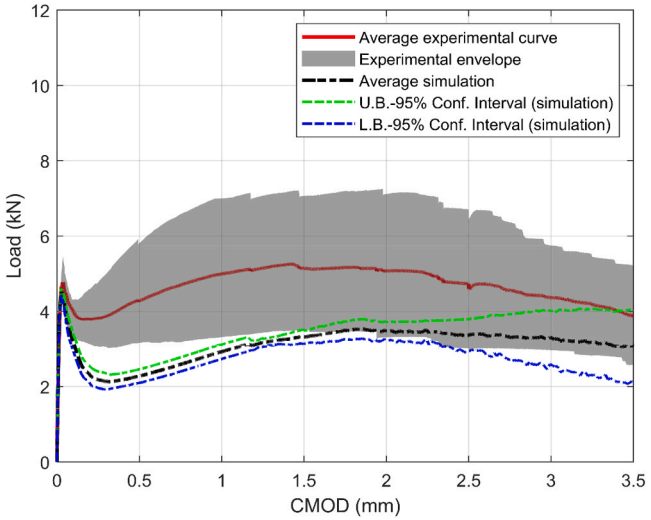

Fig. 21. Experimental and simulation (random orientation) results of load-CMOD curves of notched SFR-SCC beams.

diagrams. Notably, these figures reveal distinct behavioural patterns: the simulations primarily exhibit deflection-softening behaviour, which contrasts with the deflection-hardening behaviour observed in experimental tests. This contrast highlights the discrepancies arising from the simplifications involved in modelling fibre orientation. The numerical simulation of flexural strength and post-cracking parameters using

random orientation in SCC tends to underestimate the results. To simulate the post-cracking behaviour of SFR-SCC with a high degree of accuracy, the orientation of fibres plays a crucial role. Although the simulation using random fibre orientation can predict the general trend, it does so with low accuracy, particularly underestimating post-cracking parameters in SCC. This divergence can be partly attributed to the modelling assumptions used in simulating randomly oriented fibres. Numerical models typically assume fibres are uniformly distributed and randomly oriented. In reality, fibres within SCC may align along the flow direction during casting, providing greater resistance to cracking and deflection than the simulated random orientation predicts. This highlights the need to account for fibre orientation influenced by the flow of SCC to improve the accuracy of numerical simulations.

To achieve high accuracy in simulating the post-cracking behaviour of SFR-SCC, it is essential to incorporate more realistic fibre orientation models that consider the flow-induced alignment during casting. Moreover, obtaining fibre orientation data from hardened concrete using techniques such as CT scanning can provide valuable insights into the actual fibre orientation, further enhancing the reliability of numerical predictions in structural applications.

4.5. *Effect of the aligned orientation of fibre*

Investigating the effect of fibre orientation, where all fibres are aligned longitudinally along the length of the prism and parallel to the loading direction, assesses its potential in maximizing flexural strength, toughness, and overall post-peak behaviour. Fig. 22 shows the load-deflection curve of the numerical simulation. The use of aligned fibres significantly enhances the load-bearing capacity and residual strength of SFR-SCC. The substantial effect of fibre orientation on the peak load and toughness of SFR-SCC is represented in Fig. 23 and Fig. 24 respectively.

When comparing the random and aligned fibre orientations, the peak load and toughness improve substantially by approximately 104.4 % and 127.1 %, respectively. This significant increase highlights the critical role of fibre alignment in enhancing the flexural strength and toughness of SFR-SCC, emphasizing the importance of optimizing fibre orientation in design applications that are primarily subjected to unidirectional loads to achieve superior mechanical performance.

The efficacy of random orientation, in terms of toughness up to a deflection of 2.667 mm, is around 44.03 % when the efficiency of aligned orientation is considered to be 100 %. This reduction in effectiveness can be corroborated by literature, indicating that the effectiveness of these fibres decreases from 100 % when aligned parallel to the tensile stress to approximately 30 % in scenarios of random distribution.

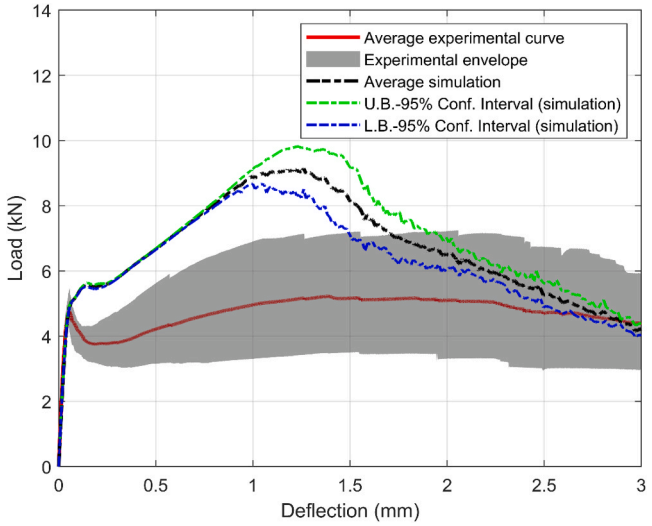

Fig. 22. Simulation results of load-deflection curves (aligned orientation).

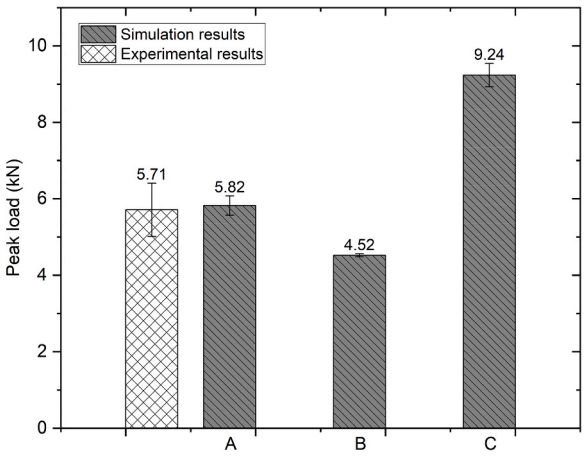

Fig. 23. Peak Load values of SCC from experiments and simulations with different fibre orientations: A) flow-based, B) random, C) aligned.

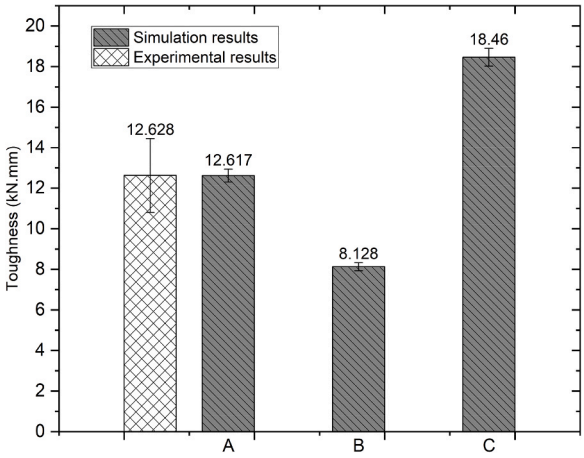

Fig. 24. Toughness values of SCC from experiments and simulations with different fibre orientations: A) flow-based, B) random, C) aligned.

5. Conclusion

Evaluating the structural integrity of concrete reinforced with steel fibres goes beyond mere strength parameters, emphasizing the necessity to consider residual tensile strength and post-peak characteristics. This study introduced a novel and practical discrete finite element modelling approach to accurately simulate the flexural properties and post-cracking performance of steel fibre-reinforced self-compacting concrete (SFR-SCC). The key findings from this study can be summarised as follows:

1. The concrete matrix was modelled using the concrete damage plasticity model in ABAQUS. Numerical simulations validated using three-point bending tests on notched prisms closely matched the experimental results, exhibiting minimal discrepancies. Specifically, the error between experimental and simulation results for plain SCC included peak load errors at 4.2 %, deflection at peak load at 5.57 %, CMOD at peak load at 9.04 %, and toughness at 1.5 %. This high degree of accuracy ensures that the model can serve as a reliable foundation for further exploration of the more complex behaviour of SFR-SCC.
2. Steel fibres were integrated as discrete truss elements within the matrix, enhancing the simulation's ability to depict individual fibre

contributions and interactions. To simulate the reinforcing effect of hooked steel fibres, laws governing pull-out force and slip, developed from an analytical model, are applied to each fibre based on its orientation relative to the cracked surface. The distribution and orientation of steel fibre was programmed in python script and imported to ABAQUS.

3. The numerical models effectively assessed damage and predicted post-peak parameters. In the simulation of SFR-SCC based on flow orientation, the discrepancies between experimental and simulation results were minimal, with a 1.93 % error for peak load and 0.09 % for toughness. The close alignment of numerical simulation results with experimental data for post-peak loads and toughness demonstrates the model's robustness and its potential for application in large structural analyses.

CRediT authorship contribution statement

Abdullah Alshahrani: Writing – review & editing, Writing – original draft, Visualization, Validation, Supervision, Software, Project administration, Methodology, Investigation, Funding acquisition, Formal analysis, Data curation, Conceptualization. **Sivakumar Kulasegaram:** Writing – review & editing, Supervision, Software, Resources. **Abhishek Kundu:** Writing – review & editing, Supervision.

Declaration of Competing Interest

The authors declare that they have no known competing financial interests or personal relationships that could have appeared to influence the work reported in this paper.

Acknowledgements

The authors are thankful to the Deanship of Graduate Studies and Scientific Research at Najran University for funding this work under the Easy Funding Program grant code (NU/EFP/SERC/13/91). In addition, the authors gratefully acknowledge the support of the Supercomputing Wales project, which is partially funded by the European Regional Development Fund (ERDF) through the Welsh Government.

Data Availability

Data will be made available on request.

References

[1] R. Deeb, B.L. Karihaloo, S. Kulasegaram, Reorientation of short steel fibres during the flow of self-compacting concrete mix and determination of the fibre orientation factor, Cem. Concr. Res. 56 (2014) 112–120, https://doi.org/10.1016/j.cemconres.2013.10.002.
[2] A. Alshahrani, S. Kulasegaram, A. Kundu, Elastic modulus of self-compacting fibre reinforced concrete: experimental approach and multi-scale simulation, Case Stud. Constr. Mater. 18 (2023), https://doi.org/10.1016/j.cscm.2022.e01723.
[3] M. Pająk, T. Ponikiewski, Flexural behavior of self-compacting concrete reinforced with different types of steel fibers, Constr. Build. Mater. 47 (2013) 397–408, https://doi.org/10.1016/j.conbuildmat.2013.05.072.
[4] ACI Committee 318., American Concrete Institute., International Organization for Standardization., Building code requirements for structural concrete (ACI 318-08) and commentary, American Concrete Institute, 2007.
[5] National Research Council, CNR-DT 204: Guide for the Design and Construction of Fiber-Reinforced Concrete Structures, 2006.
[6] RILEM TC 162-TDF, Rilem TC 162-TDF: test and design methods for steel fibre reinforced concrete - Bending test (Final Recommendation), Mater. Struct. /Mater. Et. Constr. 35 (2002) 579–582, https://doi.org/10.1617/13884.
[7] AS5100.5:2017, Bridge design Part 5: Concrete, Australian Standards (2017).
[8] FIB, Fib Model Code for Concrete Structures 2010, Lausanne, Switzerland, 2013.
[9] JSCE Concrete Committee, Standard Specifications for Concrete Structures, 2007. https://doi.org/10.3151/coj1975.46.7_3.
[10] Z. Wu, C. Shi, K.H. Khayat, Investigation of mechanical properties and shrinkage of ultra-high performance concrete: influence of steel fiber content and shape, Compos B Eng. 174 (2019) 107021, https://doi.org/10.1016/j.compositesb.2019.107021.
[11] A. Alshahrani, S. Kulasegaram, Effect of fibre diameter and tensile strength on the mechanical, fracture, and fibre distribution properties of eco-friendly high-strength self-compacting concrete, Constr. Build. Mater. 403 (2023) 133161, https://doi.org/10.1016/j.conbuildmat.2023.133161.
[12] L. Candido, F. Micelli, Seismic behaviour of regular reinforced concrete plane frames with fiber reinforced concrete in joints, Bull. Earthq. Eng. 16 (2018) 4107–4132, https://doi.org/10.1007/s10518-018-0325-9.
[13] C.E. Chalioris, P.M.K. Kosmidou, C.G. Karayannis, Cyclic response of steel fiber reinforced concrete slender beams: an experimental study, Materials 12 (2019), https://doi.org/10.3390/ma12091398.
[14] C.E. Chalioris, C.G. Karayannis, Effectiveness of the use of steel fibres on the torsional behaviour of flanged concrete beams, Cem. Concr. Compos 31 (2009) 331–341, https://doi.org/10.1016/j.cemconcomp.2009.02.007.
[15] L. Ferrara, Y.-D. Park, S.P. Shah, Correlation among fresh state behavior. Fiber Dispersion, and Toughness Properties of SFRCs, American Society of Civil Engineers, 2008, pp. 493–501, https://doi.org/10.1061/ASCE0899-1561200820:7493.
[16] S. Lim, R.A. Raju, M. Matsuda, T. Okamoto, M. Akiyama, Structural behavior prediction of SFRC beams by a novel integrated approach of X-ray imaging and finite element method, Constr. Build. Mater. 170 (2018) 347–365, https://doi.org/10.1016/j.conbuildmat.2018.03.079.
[17] R.A. Raju, S. Lim, M. Akiyama, T. Kageyama, Effects of concrete flow on the distribution and orientation of fibers and flexural behavior of steel fiber-reinforced self-compacting concrete beams, Constr. Build. Mater. 262 (2020) 119963, https://doi.org/10.1016/j.conbuildmat.2020.119963.
[18] M.G. Alberti, A. Enfedaque, J.C. Gálvez, Fracture mechanics of polyolefin fibre reinforced concrete: study of the influence of the concrete properties, casting procedures, the fibre length and specimen size, Eng. Fract. Mech. 154 (2016) 225–244, https://doi.org/10.1016/j.engfracmech.2015.12.032.
[19] S. Zhang, L. Liao, S. Song, C. Zhang, Experimental and analytical study of the fibre distribution in SFRC: a comparison between image processing and the inductive test, Compos Struct. 188 (2018) 78–88, https://doi.org/10.1016/j.compstruct.2018.01.006.
[20] A. Abrishambaf, J.A.O. Barros, V.M.C.F. Cunha, Relation between fibre distribution and post-cracking behaviour in steel fibre reinforced self-compacting concrete panels, Cem. Concr. Res. 51 (2013) 57–66, https://doi.org/10.1016/j.cemconres.2013.04.009.
[21] M.Di Prisco, FRC: Structural applications and standards, Mater. Struct. /Mater. Et. Constr. 42 (2009) 1169–1171, https://doi.org/10.1617/s11527-009-9545-4.
[22] P. Serna, S. Arango, T. Ribeiro, A.M. Núñez, E. Garcia-Taengua, Structural cast-in-place SFRC: Technology, control criteria and recent applications in spain, Mater. Struct. /Mater. Et. Constr. 42 (2009) 1233–1246, https://doi.org/10.1617/s11527-009-9540-9.
[23] B. Boulekbache, M. Hamrat, M. Chemrouk, S. Amziane, Flowability of fibre-reinforced concrete and its effect on the mechanical properties of the material, Constr. Build. Mater. 24 (2010) 1664–1671, https://doi.org/10.1016/j.conbuildmat.2010.02.025.
[24] Y. Huang, J. Huang, W. Zhang, X. Liu, Experimental and numerical study of hooked-end steel fiber-reinforced concrete based on the meso- and macro-models, Compos Struct. 309 (2023), https://doi.org/10.1016/j.compstruct.2023.116750.
[25] P. Robins, S. Austin, P. Jones, Pull-out behaviour of hooked steel fibres, Mater. Struct. /Mater. Et. Constr. 35 (2002) 434–442, https://doi.org/10.1007/bf02483148.
[26] T. Soetens, A. Van Gysel, S. Matthys, L. Taerwe, A semi-analytical model to predict the pull-out behaviour of inclined hooked-end steel fibres, Constr. Build. Mater. 43 (2013) 253–265, https://doi.org/10.1016/j.conbuildmat.2013.01.034.
[27] I.I. Bashar, A.B. Sturm, P. Visintin, A.H. Sheikh, Analytical approach to quantify the pull-out behaviour of hooked end steel fibres, Aust. J. Civ. Eng. 00 (2022) 1–21, https://doi.org/10.1080/14488353.2022.2117338.
[28] F. Laranjeira, C. Molins, A. Aguado, Predicting the pullout response of inclined hooked steel fibers, Cem. Concr. Res. 40 (2010) 1471–1487, https://doi.org/10.1016/j.cemconres.2010.05.005.
[29] F. Laranjeira, A. Aguado, C. Molins, Predicting the pullout response of inclined straight steel fibers, Mater. Struct. /Mater. Et. Constr. 43 (2010) 875–895, https://doi.org/10.1617/s11527-009-9553-4.
[30] R. Breitenbücher, G. Meschke, F. Song, Y. Zhan, Experimental, analytical and numerical analysis of the pullout behaviour of steel fibres considering different fibre types, inclinations and concrete strengths, Struct. Concr. 15 (2014) 126–135, https://doi.org/10.1002/suco.201300058.
[31] J.J. Kim, D.Y. Yoo, Effects of fiber shape and distance on the pullout behavior of steel fibers embedded in ultra-high-performance concrete, Cem. Concr. Compos 103 (2019) 213–223, https://doi.org/10.1016/j.cemconcomp.2019.05.006.
[32] A. Sarraz, H. Nakamura, T. Kanakubo, T. Miura, H. Kobayashi, Bond behavior simulation of deformed rebar in fiber-reinforced cementitious composites using three-dimensional meso-scale model, Cem. Concr. Compos 131 (2022) 104589, https://doi.org/10.1016/j.cemconcomp.2022.104589.
[33] F. Isla, P. Argañaraz, B. Luccioni, Numerical modelling of steel fibers pull-out from cementitious matrixes, Constr. Build. Mater. 332 (2022), https://doi.org/10.1016/j.conbuildmat.2022.127373.
[34] J. Qi, Z. Wu, Z.J. Ma, J. Wang, Pullout behavior of straight and hooked-end steel fibers in UHPC matrix with various embedded angles, Constr. Build. Mater. 191 (2018) 764–774, https://doi.org/10.1016/j.conbuildmat.2018.10.067.
[35] F. Isla, G. Ruano, B. Luccioni, Analysis of steel fibers pull-out, Exp. Study, Constr. Build. Mater. 100 (2015) 183–193, https://doi.org/10.1016/j.conbuildmat.2015.09.034.

[36] E. Zile, O. Zile, Effect of the fiber geometry on the pullout response of mechanically deformed steel fibers, Cem. Concr. Res. 44 (2013) 18–24, https://doi.org/10.1016/j.cemconres.2012.10.014.
[37] H. Zhang, Y.J. Huang, Z.J. Yang, S.L. Xu, X.W. Chen, A discrete-continuum coupled finite element modelling approach for fibre reinforced concrete, Cem. Concr. Res. 106 (2018) 130–143, https://doi.org/10.1016/j.cemconres.2018.01.010.
[38] M.L.R. Mineiro, R. Monte, O.L. Manzoli, L.A.G. Bitencourt, An integrated experimental and multiscale numerical methodology for modeling pullout of hooked-end steel fiber from cementitious matrix, Constr. Build. Mater. 344 (2022), https://doi.org/10.1016/j.conbuildmat.2022.128215.
[39] Y. Zhan, H.G. Bui, J. Ninic, S.A. Mohseni, G. Meschke, Numerical modeling of steel Fiber Reinforced Concrete on the meso- and macro-scale, Comput. Model. Concr. Struct. Proc. Eur.-C. 2014 (1) (2014) 579–586, https://doi.org/10.1201/b16645-64.
[40] Y. Deng, Z. Zhang, C. Shi, Z. Wu, C. Zhang, Steel fiber–matrix interfacial bond in ultra-high performance concrete: a review, Engineering 22 (2023) 215–232, https://doi.org/10.1016/j.eng.2021.11.019.
[41] D.Y. Yoo, S. Kim, J.J. Kim, B. Chun, An experimental study on pullout and tensile behavior of ultra-high-performance concrete reinforced with various steel fibers, Constr. Build. Mater. 206 (2019) 46–61, https://doi.org/10.1016/j.conbuildmat.2019.02.058.
[42] L. Huo, J. Bi, Y. Zhao, Z. Wang, Constitutive model of steel fiber reinforced concrete by coupling the fiber inclining and spacing effect, Constr. Build. Mater. 280 (2021) 122423, https://doi.org/10.1016/j.conbuildmat.2021.122423.
[43] H. Singh, Steel Fiber Reinforced Concrete Behavior, Modelling and Design, 2017. ⟨http://www.jsce.or.jp/committee/concrete/e/newsletter/newsletter05/JSCE-VIFCEA⟩ Joint Seminar Papers.htm%0Ahttp://pubsindex.trb.org/view.aspx?id= 25485.
[44] Y. Chi, M. Yu, L. Huang, L. Xu, Finite element modeling of steel-polypropylene hybrid fiber reinforced concrete using modified concrete damaged plasticity, Eng. Struct. 148 (2017) 23–35, https://doi.org/10.1016/j.engstruct.2017.06.039.
[45] J. Bi, L. Huo, Y. Zhao, H. Qiao, Modified the smeared crack constitutive model of fiber reinforced concrete under uniaxial loading, Constr. Build. Mater. 250 (2020) 118916, https://doi.org/10.1016/j.conbuildmat.2020.118916.
[46] G. Etse, A. Caggiano, S. Vrech, Multiscale failure analysis of fiber reinforced concrete based on a discrete crack model, Int. J. Fract. 178 (2012) 131–146, https://doi.org/10.1007/s10704-012-9733-z.
[47] S. Khaleel Ibrahim, N. Abbas Hadi, M. Movahedi Rad, Experimental and numerical analysis of steel-polypropylene hybrid fibre reinforced concrete deep beams, Polymers 15 (2023), https://doi.org/10.3390/polym15102340.
[48] Z. Xu, H. Hao, H.N. Li, Mesoscale modelling of dynamic tensile behaviour of fibre reinforced concrete with spiral fibres, Cem. Concr. Res. 42 (2012) 1475–1493, https://doi.org/10.1016/j.cemconres.2012.07.006.
[49] V.M.C.F. Cunha, J.A.O. Barros, J.M. Sena-Cruz, A finite element model with discrete embedded elements for fibre reinforced composites, Comput. Struct. 94–95 (2012) 22–33, https://doi.org/10.1016/j.compstruc.2011.12.005.
[50] V.M.C.F. Cunha, J.A.O. Barros, J.M. Sena-Cruz, An integrated approach for modelling the tensile behaviour of steel fibre reinforced self-compacting concrete, Cem. Concr. Res. 41 (2011) 64–76, https://doi.org/10.1016/j.cemconres.2010.09.007.
[51] R.C. Yu, H. Cifuentes, I. Rivero, G. Ruiz, X. Zhang, Dynamic fracture behaviour in fibre-reinforced cementitious composites, J. Mech. Phys. Solids 93 (2016) 135–152, https://doi.org/10.1016/j.jmps.2015.12.025.
[52] C. Octávio, D. Dias-da-Costa, J. Alfaiate, E. Júlio, Modelling the behaviour of steel fibre reinforced concrete using a discrete strong discontinuity approach, Eng. Fract. Mech. 154 (2016) 12–23, https://doi.org/10.1016/j.engfracmech.2016.01.006.
[53] Y.T. Trindade, L.A.G. Bitencourt, R. Monte, A.D. de Figueiredo, O.L. Manzoli, Design of SFRC members aided by a multiscale model: Part I – predicting the post-cracking parameters, Compos Struct. 241 (2020), https://doi.org/10.1016/j.compstruct.2020.112078.
[54] Y. Zhao, J. Bi, L. Huo, Z. Wang, J. Guan, Y. Zhao, Development of a coupled numerical framework of steel fiber reinforced self-compacting concrete, Constr. Build. Mater. 303 (2021) 124582, https://doi.org/10.1016/j.conbuildmat.2021.124582.
[55] A. Pros, P. Diez, M. Climent, Modeling steel fiber reinforced concrete: numerical immersed boundary approach and a phenomenological mesomodel for concrete-fiber interaction, Int. J. Numer. Methods Eng. (2012) 65–86, https://doi.org/10.1002/nme.
[56] L. Martinie, N. Roussel, Simple tools for fiber orientation prediction in industrial practice, Cem. Concr. Res. 41 (2011) 993–1000, https://doi.org/10.1016/j.cemconres.2011.05.008.
[57] S. Zhang, C. Zhang, L. Liao, C. Wang, R. Zhao, Investigation into the effect of fibre distribution on the post-cracking tensile strength of SFRC through physical experimentation and numerical simulation, Constr. Build. Mater. 248 (2020) 118433, https://doi.org/10.1016/j.conbuildmat.2020.118433.
[58] B. Marks, M. Miletić, B.C.H. Lee, M.H. Zia, J.A.O. Barros, D. Dias-da-Costa, Monitoring steel fibre orientation in self-compacting cementitious composite slabs during pouring with dynamic X-ray radiography, Cem. Concr. Res. 143 (2021), https://doi.org/10.1016/j.cemconres.2021.106390.
[59] T. Ponikiewski, J. Katzer, M. Bugdol, M. Rudzki, Steel fibre spacing in self-compacting concrete precast walls by X-ray computed tomography, Mater. Struct. /Mater. Et. Constr. 48 (2015) 3863–3874, https://doi.org/10.1617/s11527-014-0444-y.
[60] Y. Zhao, J. Bi, Z. Wang, L. Huo, J. Guan, Y. Zhao, Y. Sun, Numerical simulation of the casting process of steel fiber reinforced self-compacting concrete: influence of material and casting parameters on fiber orientation and distribution, Constr. Build. Mater. 312 (2021) 125337, https://doi.org/10.1016/j.conbuildmat.2021.125337.
[61] A. Amin, S.J. Foster, Predicting the flexural response of steel fibre reinforced concrete prisms using a sectional model, Cem. Concr. Compos 67 (2016) 1–11, https://doi.org/10.1016/j.cemconcomp.2015.12.007.
[62] M.C. Nataraja, N. Dhang, A.P. Gupta, Toughness characterization of steel fiber-reinforced concrete by JSCE approach, 2000.
[63] G. Giaccio, J.M. Tobes, R. Zerbino, Use of small beams to obtain design parameters of fibre reinforced concrete, Cem. Concr. Compos 30 (2008) 297–306, https://doi.org/10.1016/j.cemconcomp.2007.10.004.
[64] W. Huang, B. Huang, A. Pan, Q. Chen, Q. Huang, R. Xu, Y. Yang, F. Xue, Numerical statistics-based research on the spatial distribution of cylindrical fiber in ideal simulated fiber reinforced concrete matrix, Constr. Build. Mater. 379 (2023) 131209, https://doi.org/10.1016/j.conbuildmat.2023.131209.
[65] S.K. Kirthika, S.K. Singh, A. Chourasia, Alternative fine aggregates in production of sustainable concrete- a review, J. Clean. Prod. 268 (2020), https://doi.org/10.1016/j.jclepro.2020.122089.
[66] M.S. Abo Dhaheer, M.M. Al-Rubaye, W.S. Alyhya, B.L. Karihaloo, S. Kulasegaram, Proportioning of self-compacting concrete mixes based on target plastic viscosity and compressive strength: Part II - experimental validation, J. Sustain Cem. Based Mater. 5 (2016) 217–232, https://doi.org/10.1080/21650373.2015.1036952.
[67] A. Alshahrani, T. Cui, A. Almutlaqah, S. Kulasegaram, Designing sustainable high-strength self- compacting concrete with high content of supplementary cementitious materials, Eur. J. Environ. Civ. Eng. 27 (2023) 1–20, https://doi.org/10.1080/19648189.2023.2279563.
[68] R. Deeb, B.L. Karihaloo, Mix proportioning of self-compacting normal and high-strength concretes, Mag. Concr. Res. 65 (2013) 546–556, https://doi.org/10.1680/macr.12.00164.
[69] BS EN 14651, Test Method for Metallic Fibre Concrete. Measuring the Flexural Tensile Strength (Limit of Proportionality (LOP), Residual), (2007).
[70] M. Ghasemi, M.R. Ghasemi, S.R. Mousavi, Studying the fracture parameters and size effect of steel fiber-reinforced self-compacting concrete, Constr. Build. Mater. 201 (2019) 447–460, https://doi.org/10.1016/j.conbuildmat.2018.12.172.
[71] S. Grunewald, Performance-Based Design of Self-compacting Fibre Reinforced Concrete, Delft University Press, Delft (The Netherlands), 2004. ⟨http://repository.tudelft.nl/view/ir/uuid:07a817aa-cba1-4c93-bbed-40a5645cf0f1/⟩.
[72] BS EN 12350-8, 12350-8 Testing fresh concrete, Self-Compacting Concrete. Slump-Flow Test (2010) 18.
[73] BS EN 12350-12, 12350-12 Testing fresh concrete, Self-Compacting Concrete. J-Ring Test (2010) 18.
[74] BS EN 12390-3, Testing Hardened Concrete: Compressive Strength of Test Specimens, (2009).
[75] BS EN 12390-13, Determination of Secant Modulus of Elasticity in Compression, (2019).
[76] RILEM FMC-50, Determination of the fracture energy of mortar and concrete by means of three-point bend tests on notched beams, Mater. Struct. 18 (1985) 285–290.
[77] ASTM C1609, Standard Test Method for Flexural Performance of Fiber Reinforced Concrete (Using Beam with Third-point Loading), (2007) 1–8.
[78] JCI-S-002-2003, Method of Test for Load-Displacement Curve of Fiber Reinforced Concrete by Use of Notched Beam, Japan Concrete Institute Standard Method (2003) 1–6.
[79] J. Lubliner, O. Javier, S. Oller, O. Eugenio, A plastic-damage model for concrete, Int. J. Solids Struct. 25 (1989) 299–326, https://doi.org/10.1016/0020-7683(89)90050-4.
[80] J. Lee, G.L. Fenves, Plastic-damage model for cyclic loading of concrete structures, J. Eng. Mech. 124 (1998) 892–900, https://doi.org/10.1061/(asce)0733-9399(1998)124:8(892).
[81] T. Yu, J.G. Teng, Y.L. Wong, S.L. Dong, Finite element modeling of confined concrete-II: plastic-damage model, Eng. Struct. 32 (2010) 680–691, https://doi.org/10.1016/j.engstruct.2009.11.013.
[82] G.G. Triantafyllou, T.C. Rousakis, A.I. Karabinis, Corroded RC beams patch repaired and strengthened in flexure with fiber-reinforced polymer laminates, Compos B Eng. 112 (2017) 125–136, https://doi.org/10.1016/j.compositesb.2016.12.032.
[83] U. Cicekli, G.Z. Voyiadjis, R.K.Abu Al-Rub, A plasticity and anisotropic damage model for plain concrete, Int. J. Plast. 23 (2007) 1874–1900, https://doi.org/10.1016/j.ijplas.2007.03.006.
[84] Commitee for The Model Code 1990, CEB Bulletin No. 213/214: CEB-FIP Model Code 90, Thomas Telford Ltd. Thomas Telford Bookshop Institution of Civil Engineers (1993) 460.
[85] S. Popovics, A numerical approach to the complete stress-strain curve of concrete, Cem. Concr. Res. 3 (1973) 583–599.
[86] FIB, Constitutive modelling of high strength / high performance concrete, Lausanne, Switzerland, 2008.
[87] H. Madkour, M. Maher, O. Ali, Finite element analysis for interior slab-column connections reinforced with GFRP bars using damage plasticity model, J. Build. Eng. 48 (2022) 104013, https://doi.org/10.1016/j.jobe.2022.104013.
[88] A.S. Genikomsou, M.A. Polak, Finite element analysis of punching shear of concrete slabs using damaged plasticity model in ABAQUS, Eng. Struct. 98 (2015) 38–48, https://doi.org/10.1016/j.engstruct.2015.04.016.
[89] D.A. Hordijk, Local Approach to Fatigue of Concrete, Delft University of Technology, Delft, The Netherlands, 1991.
[90] Z.P. Bažant, B.H. Oh, Crack band theory for fracture of concrete, Mater. Struct. 16 (1983) 155–177, https://doi.org/10.1007/BF02486267, accessed January 25, 2024.

[91] A. Mathern, J. Yang, A practical finite element modeling strategy to capture cracking and crushing behavior of reinforced concrete structures, Materials 14 (2021) 1–26, https://doi.org/10.3390/ma14030506.
[92] G.M. Chen, J.F. Chen, J.G. Teng, On the finite element modelling of RC beams shear-strengthened with FRP, Constr. Build. Mater. 32 (2012) 13–26, https://doi.org/10.1016/j.conbuildmat.2010.11.101.
[93] Y. Tao, J.F. Chen, Concrete damage plasticity model for modeling FRP-to-concrete bond behavior, J. Compos. Constr. 19 (2015) 1–13, https://doi.org/10.1061/(asce)cc.1943-5614.0000482.
[94] R.Z. Alrousan, B.R. Alnemrawi, Punching shear behavior of FRP reinforced concrete slabs under different opening configurations and loading conditions, Case Stud. Constr. Mater. 17 (2022), https://doi.org/10.1016/j.cscm.2022.e01508.
[95] A. Abrishambaf, V.M.C.F. Cunha, J.A.O. Barros, A two-phase material approach to model steel fibre reinforced self-compacting concrete in panels, Eng. Fract. Mech. 162 (2016) 1–20, https://doi.org/10.1016/j.engfracmech.2016.04.043.
[96] M.Y. Yardimci, B. Baradan, M.A. Taşdemir, Effect of fine to coarse aggregate ratio on the rheology and fracture energy of steel fibre reinforced self-compacting concretes, Sadhana 39 (2014) 1447–1469, https://doi.org/10.1007/s12046-014-0257-2.